

Unprecedented Constraints on Gas Flows at High Redshift Using Deep JWST/NIRSpec Observations from the LyC22, EXCELS, and AURORA Surveys

EMILY KEHOE,¹ ALICE E. SHAPLEY,¹ ADAM C. CARNALL,² FERGUS CULLEN,² THOMAS M. STANTON,²
DANIEL SCHAEERER,^{3,4} RUI MARQUES-CHAVES,⁵ CHARLES C. STEIDEL,⁶ RYAN L. SANDERS,⁷ NATALIE LAM,¹
KARLA Z. ARELLANO-CORDOVA,⁸ RYAN BEGLEY,⁹ SOPHIA R. FLURY,² NATALIA G. GUSEVA,¹⁰ TIMOTHY HECKMAN,^{11,12}
ALAINA HENRY,¹³ AKIO K. INOUE,^{14,15} YURI I. IZOTOV,¹⁰ HO-HIN LEUNG,² DEREK J. MCLEOD,² KATE ROWLANDS,^{16,17}
ALBERTO SALDANA-LOPEZ,¹⁸ DIRK SCHOLTE,² MAYA SKARBINSKI,¹⁷ STRUAN D. STEVENSON,² ELIZABETH TAYLOR,²
BINGJIE WANG,^{19,*} AND NAVEEN A. REDDY²⁰

¹*Department of Physics & Astronomy, University of California, Los Angeles, 430 Portola Plaza, Los Angeles, CA 90095, USA*

²*Institute for Astronomy, University of Edinburgh, Royal Observatory, Edinburgh, EH9 3HJ, UK*

³*Observatoire de Genève, Université de Genève, Chemin Pegasi 51, 1290 Versoix, Switzerland*

⁴*CNRS, IRAP, 14 Avenue E. Belin, 31400 Toulouse, France*

⁵*Geneva Observatory, Department of Astronomy, University of Geneva, Chemin Pegasi 51, CH-1290 Versoix, Switzerland*

⁶*Cahill Center for Astronomy and Astrophysics, California Institute of Technology, MS 249-17, Pasadena, CA 91125, USA*

⁷*Department of Physics and Astronomy, University of Kentucky, 505 Rose Street, Lexington, KY 40506, USA*

⁸*Centro de Estudios de Física del Cosmos de Aragón (CEFCA), Plaza San Juan 1, 44001 Teruel, Spain*

⁹*Armagh Observatory and Planetarium, College Hill, Armagh, BT61 9DG, N. Ireland, UK*

¹⁰*Bogolyubov Institute for Theoretical Physics, National Academy of Sciences of Ukraine, 14-b Metrolohichna str., Kyiv, 03143, Ukraine*

¹¹*School of Earth & Space Exploration, Arizona State University, 781 Terrace Mall, Tempe, AZ 85287, USA*

¹²*Department of Physics & Astronomy, Johns Hopkins University, Bloomberg Centre, 3400 N. Charles Street, Baltimore, MD 21218, USA*

¹³*Space Telescope Science Institute, 3700 San Martin Drive, Baltimore, MD 21218, USA*

¹⁴*Waseda Research Institute for Science and Engineering, Faculty of Science and Engineering, Waseda University, 3-4-1 Okubo, Shinjuku, 169-8555 Tokyo, Japan*

¹⁵*Department of Physics, School of Advanced Science and Engineering, Faculty of Science and Engineering, Waseda University, 3-4-1 Okubo, Shinjuku, 169-8555 Tokyo, Japan*

¹⁶*AURA for ESA, Space Telescope Science Institute, 3700 San Martin Drive, Baltimore, MD 21218, USA*

¹⁷*William H. Miller III Department of Physics and Astronomy, Johns Hopkins University, Baltimore, MD 21218, USA*

¹⁸*Department of Astronomy, Oskar Klein Centre, Stockholm University, 106 91 Stockholm, Sweden*

¹⁹*Department of Astrophysical Sciences, Princeton University, Princeton, NJ 08544, USA*

²⁰*Department of Physics & Astronomy, University of California, Riverside, 900 University Avenue, Riverside, CA 92521, USA*

ABSTRACT

We investigate how low-ionization gas flows in typical star-forming galaxies at $z \sim 3$ depend on galaxy intrinsic properties and viewing angle. For this analysis we use JWST/NIRSpec observations of rest-frame near-UV Fe II and Mg II absorption, and rest-frame optical Na D absorption. This study combines galaxies from the LyC22, EXCELS, and AURORA surveys and contains 176, 197, and 315 galaxies, respectively, with Fe II, Mg II, and Na D coverage. Based on both individual and composite spectra, we find no statistically significant correlations between outflow velocity and galaxy properties. However, galaxies with detected outflows tend towards higher stellar masses, SFR, and Σ_{SFR} than those without outflows, suggesting that the two samples are not drawn from the same parent population. Finally, we additionally find that Mg II emission is preferentially detected in galaxies with lower stellar mass and A_V , and higher sSFR, consistent with conditions that favor the escape of resonantly scattered line and ionizing continuum radiation. We present the first evidence in $z \sim 3$ star-forming galaxies that properties of the absorption lines depend on galaxy inclination, with more face-on systems showing stronger absorption and higher outflow velocities, while inflowing gas is more frequently detected in more highly inclined galaxies. These trends are consistent with observations at $z \lesssim 1$ and predictions

from cosmological simulations in which galactic winds are launched perpendicular to the galactic disks, while accretion occurs primarily along the disk plane.

Keywords: galaxies: evolution – galaxies: high-redshift – galaxies: kinematics and dynamics

1. INTRODUCTION

Gas flows play a fundamental role in galaxy evolution across cosmic time by governing the baryon cycle between galaxies and their surrounding environments. These flows regulate the supply of star-forming material, redistribute metals, and enrich the circumgalactic medium (CGM) and intergalactic medium (IGM) with material expelled from the interstellar medium (ISM) (Di Matteo et al. 2005; Scannapieco et al. 2005; Hopkins et al. 2008; Somerville et al. 2008; Erb 2015; Tumlinson et al. 2017). Feedback-driven outflows powered by massive stars, supernovae, and active galactic nuclei (AGN) inject energy and momentum into the ISM and launch material into the CGM, regulating star formation (Silk & Rees 1998; Veilleux et al. 2005; Murray et al. 2011). Gas inflows replenish galaxies with fresh material that sustains star formation, establishing a continuous exchange of baryons that influences how galaxies evolve over time (Tumlinson et al. 2017; Kacprzak 2017).

Galaxy gas flows have a multiphase structure, spanning cold neutral gas, warm ionized gas, and hot X-ray emitting plasma (Heckman et al. 1990; Martin 2005; Rubin et al. 2014; Chisholm et al. 2017). These phases are traced through a wide range of diagnostics, including near-ultraviolet (NUV; 2200–3000 Å) absorption lines such as Fe II and Mg II (e.g., Weiner et al. 2009; Erb et al. 2012; Bordoloi et al. 2014), far-ultraviolet (FUV; below 2200 Å) absorption lines such as Si II, C II, Si IV, C IV, and O VI, along with resonantly scattered Ly α emission (e.g., Shapley et al. 2003; Steidel et al. 2010; Tumlinson et al. 2011; Calabrò et al. 2022), optical features including H α and [OIII] λ 5007 emission and NaD absorption (e.g., Chen et al. 2010; Förster Schreiber et al. 2019; Davies et al. 2024; Carniani et al. 2024; Saldana-Lopez et al. 2025), and X-ray observations (e.g., Strickland & Heckman 2009; Tombesi et al. 2010). Among these tracers, low-ionization absorption lines are especially useful for studying cool gas kinematics because they directly trace material moving along the line of sight through blueshifted and redshifted absorption.

The geometry of gas flows is essential for understanding how feedback and accretion operate within galaxies. Cosmological simulations predict that star formation-

driven outflows are not isotropic, but instead preferentially emerge perpendicular to the galactic disks, while inflowing gas is funneled through the galactic disk along the major axis (e.g., Brook et al. 2011; Nelson et al. 2019; Péroux et al. 2020). In this picture, the properties of the observed absorption lines depend on galaxy inclination. Observational studies across multiple emission- and absorption-line tracers spanning $0 \lesssim z \lesssim 2$ generally support this model. Outflows measured from absorption lines are often found to show stronger blueshifted signatures in more face-on systems, while inflow signatures are more frequently observed in more highly-inclined galaxies (Heckman et al. 1990; Heckman et al. 2000; Chen et al. 2010; Stewart et al. 2011; Kacprzak et al. 2012; Newman et al. 2012; Rubin et al. 2012; Roberts-Borsani & Saintonge 2019). However, the strength and consistency of these trends vary across studies, with several higher redshift ($z \gtrsim 2$) datasets suggesting no dependence of gas flow properties on inclination (Law et al. 2012; Förster Schreiber et al. 2019; Weldon et al. 2022), and indicating that such trends are more difficult to detect at earlier times.

The launch of the James Webb Space Telescope (*JWST*) has enabled a new regime for studying galactic gas flows at high redshift. Prior to *JWST*, NUV absorption features at $z > 2$ were largely inaccessible from the ground due to atmospheric absorption and limited near-infrared spectroscopic capabilities, restricting studies of NUV tracers to lower redshift galaxies. With *JWST*/NIRSpec, it is now possible to observe these features in galaxies during the peak epoch of cosmic star formation, allowing direct measurements of NUV absorption in galaxies at $z > 2$ (Kehoe et al. 2025; Lyu et al. 2026). These new probes of gas flows at $z > 2$ enable direct comparisons with trends established at lower redshifts. At the same time, *JWST* provides high-resolution images, yielding robust measurements of galaxy morphological properties, such as inclination. These measurements of galaxy orientation offer the opportunity to connect NUV inflow and outflow kinematics with galaxy inclination and therefore place new constraints on the geometry of gas flows in high-redshift galaxies.

Utilizing these new capabilities, Kehoe et al. (2025) analyzed *JWST*/NIRSpec observations from the Assembly of Ultradeep Rest-optical Observations Revealing

* NHFP Hubble Fellow

Astrophysics (AURORA) Cycle 1 *JWST*/NIRSpec program (Shapley et al. 2025). We used Fe II and Mg II absorption to study outflowing gas in star-forming galaxies at $z \gtrsim 2.5$, providing direct comparisons of trends between NUV absorption kinematics and outflow properties between low ($z \sim 1$) and high ($z > 2.5$) redshift galaxies for the first time. Kehoe et al. (2025) also demonstrated the feasibility of detecting and analyzing Na D in these high redshift galaxies.

Building on this framework, we expand the previous *JWST* sample by incorporating two additional surveys: the LyC22 Cycle 1 *JWST*/NIRSpec program (Schaerer et al. 2026) and the Early eXtragalactic Continuum and Emission Line Science (EXCELS) Cycle 2 *JWST*/NIRSpec program (Carnall et al. 2024). Including two additional surveys increases the overall sample size by a factor of four, enabling a more statistically robust exploration of NUV absorption in high redshift galaxies. With this expanded sample at $z \sim 3$, we perform a more detailed analysis of Fe II, Mg II, and Na D absorption. In particular, we investigate how outflow signatures relate to the galaxy stellar mass (M_*), star formation rate (SFR), specific star formation rate (sSFR), star formation rate surface density (Σ_{SFR}), UV slope (β), dust attenuation (A_V), and nebular $E(B-V)$. These correlations allow us to provide constraints on the physical driving mechanisms of galactic-scale outflows. We also examine trends with galaxy inclination to investigate the geometry of the flowing gas. Notably, this study provides the first statistically robust analysis on how gas flows vary with galaxy orientation, providing new constraints on the geometry of gas flows for galaxies at $z \sim 3$.

The outline of this paper is as follows. Section 2 describes the *JWST* observations and sample selection. Section 3 outlines the methods used to measure galaxy properties and outflow velocities derived from Fe II, Mg II, and Na D absorption features, and the construction of the composite spectra. Section 4 presents the results of our analysis, including correlations between outflow and absorption properties and galaxy properties, and trends with inflowing gas and galaxies with significant Mg II emission. Section 5 compares our results to previous outflow studies, discusses the geometry of inflowing and outflowing gas, and examines the connection between Mg II emission and LyC escape. Throughout this work, we assume a Λ CDM cosmology with $H_0 = 70 \text{ km s}^{-1}$, $\Omega_m = 0.3$, and $\Omega_\Lambda = 0.7$, and the Chabrier (2003) initial mass function (IMF).

2. OBSERVATIONS

In this work, we analyze a sample of galaxies with observations drawn from three different *JWST*/NIRSpec programs: the Cycle 1 LyC22 survey (GO 1869, PI: Schaerer; Schaerer et al. 2026); the Cycle 2 EXCELS survey (GO 3543; PIs: Carnall, Cullen; Carnall et al. 2024); and the Cycle 1 AURORA program (GO 1914; PIs: Shapley, Sanders; Shapley et al. 2025). We now describe each of these programs in turn, and the combined sample that we construct from them at $z_{\text{med}} = 3.07$.

2.1. The LyC22 Survey

The LyC22 Survey is described in detail in Schaerer et al. (2026). Targets were observed with the NIRSpec micro-shutter assembly (MSA) in three pointings, two of which were in the SSA22 field and one in the Westphal field. Each pointing was observed with both the G140M/F100LP and G235M/F170LP grating/filter combinations, providing wavelength coverage from 1.0 – 3.1 μm . Exposure times were 9.2 hours in G140M and 8.8 hours in G235M, corresponding, respectively, to median 3σ line flux sensitivities of $2.5 \times 10^{-19} \text{ erg cm}^{-2} \text{ s}^{-1}$ and $1.8 \times 10^{-19} \text{ erg cm}^{-2} \text{ s}^{-1}$. The LyC22 survey aims to test indirect observational proxies for Lyman continuum escape in star-forming galaxies at $z \sim 2.5 - 3.5$ (both narrowband-selected Ly α emitters and color-selected Lyman break galaxies), which is critical for models of cosmic reionization (Steidel et al. 2018). A total of 143 galaxies was targeted with LyC22, of which 117 yielded spectroscopic redshifts with NIRSpec and spanned the range $z = 0.07 - 4.04$. LyC22 targets are also covered by extensive multi-wavelength photometry, including both ground-based data as well as imaging from the Hubble Space Telescope (*HST*)/ACS and *HST*/WFC3, and *JWST*/NIRCam. LyC22 data reduction is described in detail in Schaerer et al. (2026), including important corrections for slit-losses.

2.2. The EXCELS Survey

The EXCELS survey was first described in Carnall et al. (2024). This NIRSpec MSA program consists of four pointings in the PRIMER UDS field, each of which was observed with the G140M/F100LP, G235M/F170LP, and G395M/F290LP grating/filter combinations. This set-up provides wavelength coverage from 1–5 μm . However, distinct MSA configurations were designed for each grating within each pointing in order to maximize the number of galaxies with coverage of key rest-UV and rest-optical features. Integration times were 4 hours in G140M and G395M and 5.5 hours in G235M, yielding slightly shallower emission-line sensitivities than LyC22 in G140M ($\times 0.65$) and G235M ($\times 0.79$) and a depth in G395M comparable to the depth

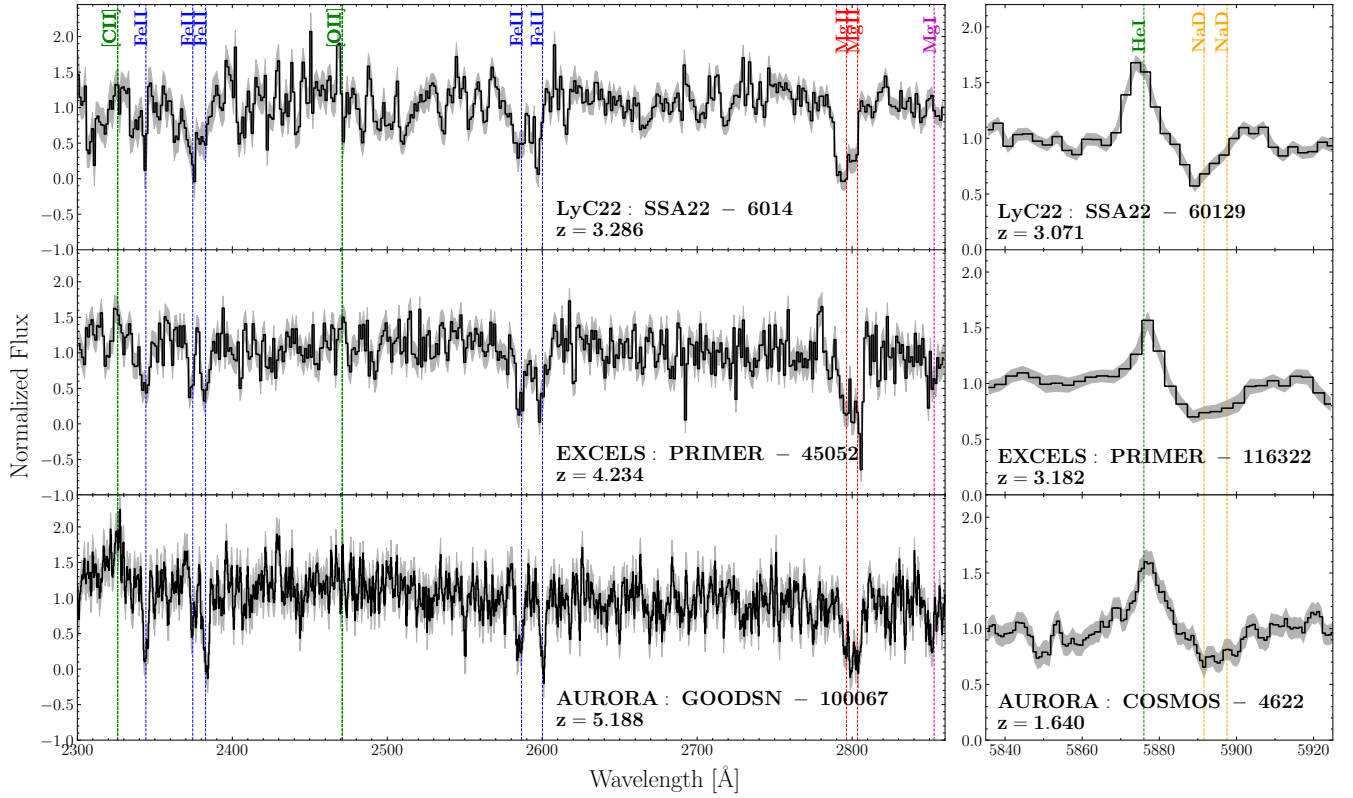


Figure 1. Rest-frame continuum-normalized spectra from the LyC22 survey (top), the EXCELS survey (middle), and the AURORA survey (bottom). Left panels show the NUV lines analyzed, with Fe II rest wavelengths indicated in blue and Mg II in red. Green lines mark emission lines not included in the analysis, and the magenta line marks the Mg I $\lambda 2850\text{\AA}$ absorption line. Right panels show example Na D profiles, with orange lines indicating the Na D $\lambda\lambda 5891, 5897\text{\AA}$ lines and the green line labeling the He I $\lambda 5875\text{\AA}$ emission line.

of the LyC22 observations in G140M and G235M. The 401 EXCELS targets included a mixture of quiescent galaxies at $z = 1-5$ and star-forming galaxies at $z \geq 0.5$, and a total of 341 secure spectroscopic redshifts were obtained with NIRSpec. EXCELS targets are covered by extensive photometric data, including both *HST*/ACS and *JWST*/NIRCam and *JWST*/MIRI F770W imaging (Carnall et al. 2024). We refer readers to Stanton et al. (2026) and Carnall et al. (2024) for a detailed description of the data reduction methods in the EXCELS survey, including the method for slit-loss corrections.

2.3. The AURORA Survey

The AURORA Survey is described in detail in e.g., Shapley et al. (2025) and Sanders et al. (2025). Briefly, this survey includes NIRSpec MSA observations of two pointings, one in the COSMOS field, and one in GOODSN. As in the EXCELS survey, AURORA observations were designed to provide wavelength coverage from $1-5 \mu\text{m}$ using the G140M/F100LP, G235M/F170LP, and G395M/F290LP grating/filter combinations. Exposures in these gratings were, respectively, 12.3, 8.0, and 4.2 hours. Therefore, the AURORA

G235M line-flux sensitivity is extremely comparable to that in LyC22, while the G140M depth is a factor of $1.14\times$ greater.

These deep exposure times were designed to detect faint auroral emission lines and determine direct, T_e -based metallicities (Sanders et al. 2026). As described in detail in Shapley et al. (2025), a total of 97 galaxies were targeted with AURORA, including 95 that yielded spectroscopic redshifts at $z = 1.4 - 10.4$. As for LyC22 and EXCELS targets, AURORA galaxies are covered by extensive multi-wavelength photometry, including ground-based, *HST*/ACS and *HST*/WFC3, and *JWST*/NIRCam data. AURORA data reduction is described in Shapley et al. (2025) and Sanders et al. (2025), including a detailed discussion of slit-loss corrections.

2.4. Combined JWST/NIRSpec Sample

From the LyC22, EXCELS and AURORA surveys, we construct a combined sample of star-forming galaxies with *JWST*/NIRSpec spectroscopy. To isolate star-forming galaxies, objects identified as AGN or quiescent are removed from the sample. In LyC22, AGN are identified from broad Balmer emission and high-ionization

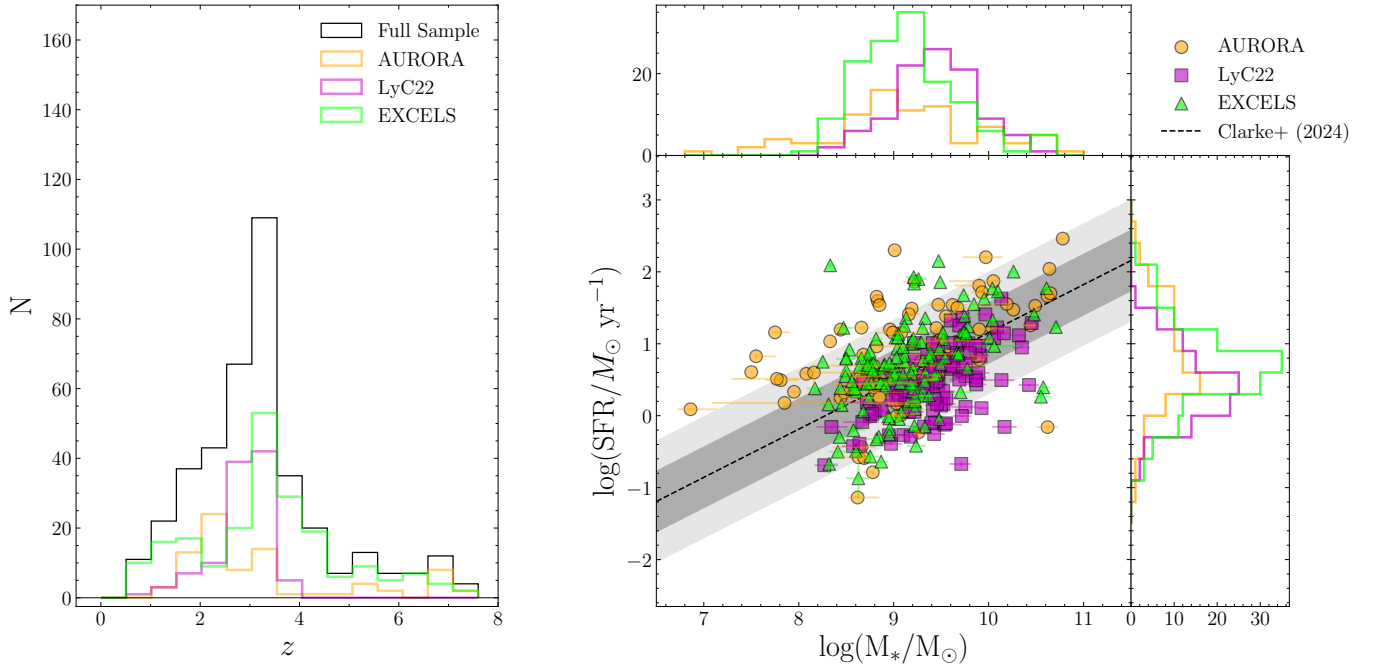


Figure 2. Properties of the *JWST* sample analyzed in this work. Left: Histogram of $H\alpha$ redshifts for the AURORA survey (orange), the LyC22 survey (magenta), the EXCELS survey (green), and the full sample (black). Right: SFR (based on $H\alpha$) vs. stellar mass for the AURORA survey (orange circles), the LyC22 survey (pink squares), and the EXCELS survey (green triangles). The SFRs are derived from dust-corrected $H\alpha$ luminosities, and the stellar mass is derived from SED fitting. The dashed line represents the star-forming main sequence for $2.7 < z \leq 4$ galaxies from Clarke et al. (2024), where the dark gray and light gray shaded regions represent the 1σ and 2σ intrinsic scatter intervals, respectively.

emission lines (Schaerer et al. 2026). In EXCELS, AGN are identified with broad Balmer emission, and quiescent galaxies are identified from best-fit SEDs showing low sSFRs and red rest-frame colors (Carnall et al. 2024). In AURORA, AGN are identified from broad Balmer lines and elevated $[N\text{II}]/H\alpha$ ratios (> 0.5), and quiescent galaxies are identified from SED fits showing suppressed star formation and spectra dominated by stellar absorption features with weak or absent nebular emission lines (Shapley et al. 2025). We further require coverage of rest-frame NUV Fe II and Mg II features, or the Na D absorption doublet (Table 1; Figure 1). The Fe II, Mg II, and Na D absorption have lower redshift limits of $z = 2.87$, $z = 2.57$, and $z = 0.70$, respectively, due to the wavelength coverage of NIRSpec.

The resulting LyC22 sample contains 67 galaxies with Fe II coverage, 81 galaxies with Mg II coverage, and 103 galaxies with Na D coverage. The EXCELS sample has 68 galaxies with Fe II coverage, 73 galaxies with Mg II coverage, and 130 galaxies with Na D coverage. In AURORA, there are 41 galaxies with Fe II coverage, 43 galaxies with Mg II coverage, 82 galaxies with Na D coverage. In total, the combined *JWST*/NIRSpec sample contains 176, 197, and 315 galaxies with Fe II, Mg II, and Na D coverage, respectively. The final sample spans $z = 0.75 - 7.57$ (median $z = 3.07$), stellar masses

$\log(M_*/M_\odot) = 6.86 - 10.78$ (median $\log(M_*/M_\odot) = 9.21$), and $H\alpha$ -derived SFRs $\log(\text{SFR}/M_\odot\text{yr}^{-1}) = -1.14 - 2.46$ (median $\log(\text{SFR}) = 0.60$) (Figure 2).

3. MEASUREMENTS

3.1. Galaxy Properties

3.1.1. SED Fitting

We determined the stellar masses (M_*) and dust attenuation values (A_V) of galaxies in our sample by fitting their spectral energy distributions (SEDs). For the LyC22 and EXCELS surveys, details of the SED fitting methodology are provided in Stanton et al. (2026), with a brief summary given here. The observed photometry was first corrected for contamination from nebular emission lines by constructing mock emission line spectra from Gaussian fits to detect lines and subtracting their contribution from each filter. We then fit the corrected photometry with the SED-fitting code BAGPIPES (Carnall et al. 2018, 2019) using Binary Population and Spectral Synthesis stellar population models (BPASS v2.21; Eldridge et al. 2017; Stanway & Eldridge 2018), which include the effects of binary stellar evolution and a Kroupa (2001) initial mass function. Star-formation histories were modeled using a delayed- τ model (i.e., $\text{SFR}(t) \sim (t - T_0) \times \exp(-(t - T_0)/\tau)$,

where T_0 is the time at the onset of star formation, stellar metallicities and masses were varied with broad ranges, and modeled with the Salim et al. (2018) flexible attenuation law. To account for the remaining nebular continuum, we included a continuum component and varied its strength through the ionization parameter, which was allowed to vary freely in the fitting process. The photometric dataset for the EXCELS sample is described in detail in Carnall et al. (2024). Photometry for the LyC22 sample consisted of a mixture of ground-based, *Spitzer*, *HST* and *JWST* bands, which was slightly different for the SSA22 and Westphal fields. The SSA22 filter set included ground-based u , B , G , V , Rs , i , z , J , H , and Ks bands, *HST*/WFC3 $F160W$, and *JWST*/NIRCam $F150W$ and $F277W$, whereas the Westphal photometry included ground-based u , g , r , i , z , J , H , Ks bands, *Spitzer*/IRAC channels 1, 2, 3, and 4, *HST*/ACS $F606W$, *HST*/WFC3 $F125W$ and $F160W$, and *JWST*/NIRCam $F277W$.

For the AURORA survey, Sanders et al. (2025) provide details of the SED modeling, including the photometric bands that were utilized. To summarize briefly, we first corrected the photometry for contributions from strong nebular emission lines and nebular continuum emission, and then performed SED fitting using this corrected photometry. The photometric measurements were drawn from the DAWN *JWST* Archive (DJA) (Valentino et al. 2023), which provided coverage from *JWST*/NIRCam (Eisenstein et al. 2026) as well as *HST*/WFC3 and *HST*/ACS imaging, giving broad wavelength coverage of each galaxy’s SED. We derived the stellar population properties and the stellar continuum by fitting flexible stellar population synthesis models (Conroy et al. 2009) to the corrected photometry using Fitting and Assessment of Synthetic Templates (FAST) (Kriek et al. 2009), with a Chabrier (2003) initial mass function and star-formation histories described by a delayed- τ model. Following earlier work (e.g., Clarke et al. 2024), we explored two sets of model assumptions, consisting of a $1.4Z_\odot$ model with the Calzetti et al. (2000) attenuation curve (the “Calzetti” model) and a $0.2Z_\odot$ model with an SMC extinction curve from Gordon et al. (2003) (the “SMC” model). For each galaxy, we adopted the solution corresponding to the minimum χ^2 value. To ensure that no significant systematics were introduced by using the existing FAST population synthesis fits for AURORA, we compared the best-fit stellar masses that would result from instead using Bagpipes models. We found excellent agreement, with a median difference of $\log(M_{*,\text{FAST}}) - \log(M_{*,\text{Bagpipes}}) = -0.03 \pm 0.22$. The joint distributions of A_V vs. M_* are also consistent when using either FAST or Bagpipes.

3.1.2. UV β Slopes

We estimated the UV continuum slope, β , which characterizes the spectral shape as $F_\lambda \propto \lambda^\beta$. β was determined by performing linear regression on the rest-frame UV photometry of each galaxy (Clarke et al. 2024). Only filters covering the rest-frame wavelength range 1250–2600 Å were included to ensure robust measurements of β . To estimate the uncertainties on β , we generated 10,000 Monte Carlo realizations of the photometry by perturbing each measurement according to its reported error. We then computed β for each realization and adopted the 16th, 50th, and 84th percentiles of the resulting distribution as the lower bound, median, and upper bound, respectively.

3.1.3. Galaxy Inclination

We calculated the galaxy inclination using,

$$\cos(i) = \frac{q^2 - \gamma^2}{1 - \gamma^2} \quad (1)$$

where q is the axis ratio that ranges between 0 and 1, and γ is the intrinsic disk thickness. We adopt $\gamma \sim 0.2$, consistent with previous studies of distant star-forming galaxies (e.g., Wisnioski et al. 2015, 2019). For the EXCELS and AURORA surveys, the axis ratios and uncertainties are a component of the Sérsic profile fits reported in the DJA morphological catalogs (Genin et al. 2025). These fits were performed using SExtractor++ (Bertin et al. 2020). Since galaxies from the LyC22 survey are not available in the DJA catalogs, we derived the axis ratios and uncertainties by modeling NIRCAM/F277W light distributions with PSF-convolved two-dimensional Gaussian fits using PySersic (Pasha & Miller 2023), where the PSF was constructed from stacked bright stars in the F277W field using PSFr (Birrer 2021; Birrer et al. 2022). As shown in Figure 3, the inclinations obtained from the DJA and PySersic measurements show similar distributions. A Kolmogorov–Smirnov (KS) test indicates that the two distributions are drawn from the same parent population, suggesting that the different fitting methodologies do not introduce a significant systematic bias.

3.1.4. Spectroscopic Measurements

We used spectroscopic detections of Balmer lines (corrected for underlying stellar absorption) to calculate the systemic redshift, star-formation rate (SFR) and nebular dust reddening ($E(B - V)_{\text{gas}}$) for galaxies in our sample. Dust attenuation was determined from the Balmer decrement, with $E(B - V)$ derived from the $H\alpha/H\beta$ flux ratio, assuming an intrinsic value of 2.79 for Case B recombination. We assumed $T_e = 15,000$ K

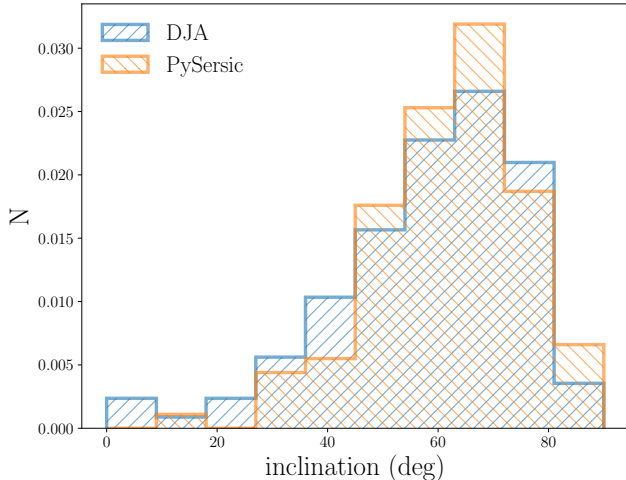


Figure 3. Normalized histograms of galaxy inclinations measured from the DJA catalogs (blue; AURORA and EXCELS) and from PySersic (orange; LyC22). Both types of measurements show similar distributions, demonstrating that the use of different methods does not introduce a significant bias.

and $n_e = 300 \text{ cm}^{-3}$, typical for star-forming galaxies at these redshifts (Topping et al. 2025; Sanders et al. 2026), and applied the Cardelli et al. (1989) dust law. In cases where $\text{H}\alpha$ was not covered by the wavelength range of the observations, the $\text{H}\gamma/\text{H}\beta$ flux ratio, with an intrinsic value of 0.475, was used. When $\text{H}\beta$ was not covered, the $\text{H}\gamma/\text{H}\alpha$ flux ratio, with an intrinsic value of 0.173, was used. The dust-corrected $\text{H}\alpha$ luminosities were then converted to SFRs using the following equation:

$$\log\left(\frac{\text{SFR}}{M_{\odot}\text{yr}^{-1}}\right) = \log\left(\frac{L_{\text{H}\alpha}}{\text{erg s}^{-1}}\right) + C \quad (2)$$

where C is a metallicity-dependent conversion factor, following Clarke et al. (2024). The conversion factor was determined from a set of BPASS models with upper mass limits of $100 M_{\odot}$ (Stanway & Eldridge 2018; Reddy et al. 2022). For the AURORA survey, galaxies fit with the “Calzetti” model had a correction factor of $C = -41.37$, and galaxies fit with the “SMC” model had a correction factor of $C = -41.59$. For the LyC22 and EXCELS surveys, which adopted different SED modeling assumptions, we applied the “SMC” model conversion factor of $C = -41.59$, following Stanton et al. (2026), who adopt this conversion and show consistency with other SFR conversion factors.

From the dust-corrected SFRs and stellar masses described above, we calculated the specific star-formation rate ($\text{sSFR} = \text{SFR}/M_*$). We also derived the star-formation rate surface density $\Sigma_{\text{SFR}} = \text{SFR}/(2\pi R_e^2)$ using the dust-corrected SFR and the galaxy’s half-light radius. For the AURORA survey, we use the methodol-

Table 1. Fitted Absorption Lines

Line	$\lambda_{\text{rest}} (\text{\AA})$	Blue Window (\AA) ^a	Red Window (\AA) ^a
Fe II	2249.88	2200 – 2220	2300 – 2330
Fe II	2260.78	2200 – 2220	2300 – 2330
Fe II	2344.21	2300 – 2330	2405 – 2425
Fe II	2374.46	2300 – 2330	2405 – 2425
Fe II	2382.77	2300 – 2330	2405 – 2425
Fe II	2586.65	2540 – 2560	2640 – 2660
Fe II	2600.17	2540 – 2560	2640 – 2660
Mg II	2796.35	2705 – 2730	2820 – 2840
Mg II	2803.53	2705 – 2730	2820 – 2840
Na D	5891.59	5810 – 5830	6000 – 6020
Na D	5897.56	5810 – 5830	6000 – 6020

^aThe blue and red regions represent the wavelength ranges used for local continuum fitting for each feature.

ogy from Pahl et al. (2022) to calculate R_e . Briefly, R_e was measured using Sérsic profile fits with *galfit*. For galaxies well described by a single Sérsic component, a circularized radius is computed using the semimajor-axis half-light radius and the axis ratio. For galaxies needing multiple Sérsic components, R_e was determined from the area containing half of the total flux. For the EXCELS survey, effective radii were adopted directly from the DJA catalogs (Valentino et al. 2023; Genin et al. 2025). For the LyC22 survey, we adopt the PSF-deconvolved effective radii from the same PySersic morphological fits described in section 3.1.3

Uncertainties in both $E(B-V)$ and SFR were quantified through Monte Carlo simulations with 10,000 realizations of the observed fluxes. For sSFR and Σ_{SFR} , we propagated the uncertainties by sampling the distributions of the underlying parameters. Specifically, sSFR uncertainties were estimated by drawing SFRs and stellar masses from Gaussian distributions defined by their measured values and associated uncertainties, computing the sSFR for each realization. Similarly, the uncertainties in Σ_{SFR} were obtained by sampling the SFRs and effective radii confidence intervals and recalculating Σ_{SFR} for each iteration.

3.2. Outflow Velocities

To characterize the kinematics of the absorbing gas, we measure the velocity offsets and equivalent widths (EWs) from Fe II, Mg II, and Na D absorption features (Table 1). These tracers probe progressively more complex line profiles, reflecting different combinations of

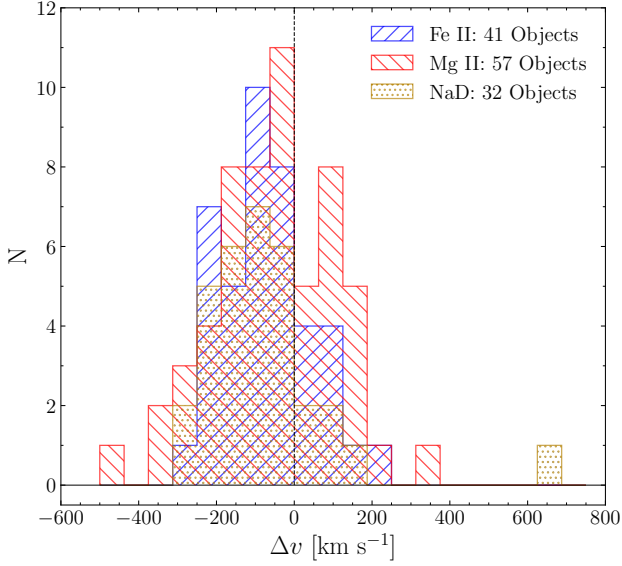


Figure 4. Histogram of the measured velocity offsets of Fe II (blue), Mg II (red), and Na D (gold) relative to the galaxy redshift from the $H\alpha$ centroid. Velocity offsets were measured for 41 galaxies using Fe II, with an average velocity of $\langle \Delta v_{\text{Fe II}} \rangle = -70 \pm 18 \text{ km s}^{-1}$, 57 galaxies using Mg II, with $\langle \Delta v_{\text{Mg II}} \rangle = -50 \pm 20 \text{ km s}^{-1}$, and 32 galaxies using Na D, with $\langle \Delta v_{\text{Na ID}} \rangle = -79 \pm 29 \text{ km s}^{-1}$.

pure absorption, emission filling, and stellar and nebular contamination, which require different modeling approaches tailored to each transition. For example, both Mg II, and Na D can be significantly affected by emission-line infilling, which is less important for Fe II (Martin et al. 2012; Zhu et al. 2015). For each tracer, we adopt the approach that most robustly reproduces the observed spectra and yields well-constrained centroid measurements.

3.2.1. Fe II

Doppler shifts in Fe II absorption lines (Table 1), provide a direct probe of large-scale galactic flows. We identified significantly detected absorption lines using a nonparametric method to estimate the line flux following the method describe in detail in Kehoe et al. (2024). In summary, we first determined the local continuum using line-free regions on the blue and red sides around each absorption feature (Table 1) determined from a high S/N composite spectrum of the full sample of galaxies with Fe II coverage (see Section 3.3 for details of composite spectra). We defined the continuum level as the average flux density of the two regions and used the continuum level to calculate the equivalent width (EW) of each line. The EW was measured by integrating over a wavelength interval extending $\pm 6 \text{ \AA}$ from the line center. This integration window was selected after

testing a range of widths, with $\pm 6 \text{ \AA}$ providing the most robust measurements while minimizing contamination from neighboring spectral features. We estimated uncertainties on the flux through Monte Carlo simulations, perturbing each spectrum by its error spectrum for 1000 realizations. A line was considered significantly detected if the flux was greater than 4σ . This threshold was determined by evaluating a range of significance levels and choosing the smallest value above 3σ that consistently produced robust results upon visual inspection.

For all detected lines, we measured the observed centroid of each line by fitting a Gaussian profile in the observed frame using a non-linear least squares fitting routine. Uncertainties were determined using the same Monte Carlo approach, where the measured centroid was taken as the mean of the realizations and the uncertainty as the standard deviation.

We calculated velocity shifts by comparing the measured centroid wavelength (λ_{obs}) to the rest wavelength of each feature (λ_{rest}):

$$\Delta v = \frac{\lambda_{\text{obs}} - \lambda_{\text{rest}}(1+z)}{\lambda_{\text{rest}}(1+z)} \times c \quad (3)$$

where z is the galaxy’s systemic redshift, determined from $H\alpha$. For galaxies with multiple detected Fe II features, we computed an inverse-variance-weighted average of the individual measurements to obtain a single velocity shift. Negative velocity offsets correspond to blueshifted absorption and may be indicative of outflowing gas, and positive velocity offsets correspond to redshifted absorption and are indicative of inflowing gas. We see instances of both outflow (blueshifted absorption) and inflow (redshifted absorption) and will discuss this in Section 5.3. In our sample, we measured Fe II velocities for 41 galaxies out of a total of 176 galaxies (23%) with Fe II coverage. The average velocity was $\langle \Delta v_{\text{Fe II}} \rangle = -70 \pm 18 \text{ km s}^{-1}$ (where the uncertainty listed is the standard error on the mean), with velocities ranging from -281 to $+213 \text{ km s}^{-1}$. The median uncertainty on individual Fe II velocity measurements was 22 km s^{-1} .

3.2.2. Mg II

The Mg II doublet $\lambda\lambda 2796, 2803$ often shows a mixture of absorption and emission, making the centroid more challenging to measure than for Fe II. To capture this complexity, we used the Markov Chain Monte Carlo (MCMC) fitting approach, `emcee` (Foreman-Mackey et al. 2013), applying the same procedure and priors as in Kehoe et al. (2025), using three different parameterizations. We first modeled the profile as an absorption doublet, with one Gaussian for each transition, then

as an emission doublet, and lastly as a four-component model that included both an emission and an absorption component for each transition (Martin et al. 2013). This method allowed us to capture the variety of Mg II profiles observed in the sample.

For each model, the spectra were restricted to the wavelength range surrounding the Mg II doublet and normalized by the continuum level, estimated from line-free regions on the blue and red sides of the line profile (Table 1). The free parameters in the fit included the centroids and widths of the Gaussian components, the integrated fluxes of each line, and the continuum level. Physically motivated priors were applied to guide the fit. For the absorption components, we constrained the flux ratio between the $\lambda 2796 \text{ \AA}$ and $\lambda 2803 \text{ \AA}$ lines to fall between 1 and 2, where a ratio of 2 corresponded to optically thin lines and a ratio of 1 indicates saturated absorption. For the emission components, the allowed flux ratio ranged from 0.8 to 2.7, as the dominant excitation mechanism sets the relative strengths of the emission lines. The flux ratio reaches values near 2 when collisional excitation dominates and decreases toward 1 when radiative excitation dominates, as both lines emitted photons with roughly equal probability. Observed line ratios often deviate from these theoretical predictions, indicating that the intervening medium consists of a mixture of uniform and porous gas that absorbs and scatters light (Martin et al. 2012, 2013; Kornei et al. 2013; Henry et al. 2018; Chisholm et al. 2020). To maintain a consistent velocity shift, we tied the centroids of the two doublet members. The absorption amplitude was also constrained, so that the lowest point of the absorption could only go 1σ below a flux density of zero. Lastly, we enforced limits on the line widths to prevent nonphysical results, requiring the Gaussian width to be at least as large as the galaxy’s velocity dispersion traced by $H\alpha$, or $H\beta$ if $H\alpha$ was not detected. When modeling Mg II as a combination of absorption and emission, the absorption and emission line widths were inferred independently.

We explored the posterior distributions using MCMC sampling, taking the median values as the best estimates of the parameters and the standard deviations as the uncertainties. The best model was selected based on χ^2 comparisons, where the two-component model (emission+absorption) was selected over the one-component model if it provided a statistically significant reduction in χ^2 (p -value < 0.01), with the p -value calculated from the difference in χ^2 based on the change in degrees of freedom between models. We set the minimum total absorption flux for Mg II to be significantly detected at 5σ . Similar to Fe II, we determined this threshold by

exploring a range of significance levels and adopting the smallest value above 3σ that produced robust results upon visual inspection. We found that 46 galaxies were best described by an absorption only fit, 2 galaxies by an emission only fit, and 11 galaxies by a combined emission and absorption fit (see Figure 3 of Kehoe et al. 2025). In total, we successfully fit Mg II profiles for 59 of the 197 galaxies (31%) with available Mg II coverage. The velocity shifts were calculated from the absorption centroids using equation 3. The average velocity for these detections was $\langle \Delta v_{\text{Mg II}} \rangle = -50 \pm 20 \text{ km s}^{-1}$, over a range of -464 to $+334 \text{ km s}^{-1}$. The median uncertainty on individual Mg II velocity measurements was 23 km s^{-1} .

3.2.3. Na D

Measuring the centroids from the Na D $\lambda\lambda 5891, 5897$ doublet is more complex than for the Fe II lines because the profile is shaped by both ISM and systemic stellar absorption components. To remove the stellar contribution, each spectrum was divided by its best-fit SED. Both the spectrum and SED were shifted into the rest frame, and the SED was interpolated onto the wavelength grid of the spectrum and locally scaled to match the continuum around the Na D doublet using continuum windows on either side of the lines (Table 1). The observed flux was then divided by the scaled SED to produce a residual spectrum dominated by ISM absorption.

The Na D profile shape is further complicated by the nearby He I $\lambda 5876 \text{ \AA}$ emission line. Therefore, both the He I emission line and Na D absorption lines must be fit simultaneously. The absorption was fit with a partial covering model from Rupke et al. (2005), where the residual flux, $F_{\text{Na D}}(\lambda_i)$, is given by

$$F_{\text{Na D}}(\lambda_i) = 1 - C_f + C_f \exp[-(\tau_b(\lambda_i) + \tau_r(\lambda_i))] \quad (4)$$

where C_f is the gas covering fraction and τ_b and τ_r are the optical depth profiles of the 5891 and 5897 absorption lines:

$$\tau_b(\lambda_i) = \tau_{0,b} \exp\left[-\frac{(\lambda_i - \lambda_c)^2}{2\sigma^2}\right], \quad (5)$$

$$\tau_r(\lambda_i) = \tau_{0,r} \exp\left[-\frac{(\lambda_i - \lambda_c - 6)^2}{2\sigma^2}\right] \quad (6)$$

where $\tau_{0,b}$ and $\tau_{0,r}$ are the central optical depths of the Na D 5891 and 5897 \AA lines, λ_c is the central wavelength of the 5891 \AA absorption line, and σ is the Gaussian width of the profile and corresponds to the velocity dispersion of the absorbing gas. Prior to our fitting, we account for the NIRSpec instrumental resolution by defining the observed line width, σ_{tot} , as

$\sigma_{\text{tot}} = \sqrt{\sigma_{\text{NaD}}^2 + \sigma_{\text{inst}}^2}$, where σ_{NaD}^2 is the intrinsic velocity width of the NaD absorption feature, and σ_{inst}^2 represents the instrumental broadening. In our model, we allow the ratio of $\tau_{0,b}/\tau_{0,r}$ to vary between 1 and 2. This range encompasses both the optically thick regime ($\tau_{0,b}/\tau_{0,r} = 1$) and the optically thin regime ($\tau_{0,b}/\tau_{0,r} = 2$). The centroids of the two lines are fixed relative to each other to ensure a consistent velocity shift across the doublet.

MCMC was used to sample the posterior distributions, where the medians were adopted as the best-fit parameters and the standard deviations as their uncertainties. Lines were considered significantly detected if the integral of the absorption profile exceeded 3σ . The threshold was determined following the same approach used for Fe II and Mg II. Furthermore, each spectrum was visually inspected due to the complexity and noisy nature of the profiles in our sample. Out of the 315 galaxies in our sample with NaD coverage, 32 had significantly detected absorption (10%). The velocity shift of NaD was calculated using the absorption centroid and equation 3. The average velocity of the sample was $\langle \Delta v_{\text{NaD}} \rangle = -79 \pm 29 \text{ km s}^{-1}$, with a range of -261 to $+664 \text{ km s}^{-1}$. The median uncertainty on individual NaD velocity measurements was 93 km s^{-1} . We summarize the velocity offsets for Fe II, Mg II and NaD in Figure 4.

3.3. Composite Spectra

The individual spectra in our sample spanned a continuum S/N per pixel range of ~ 0.4 –24 near the features of interest, with a median value of 3.5, while galaxies with reliable velocity measurements had a higher median continuum S/N of 5.6. Given the limited S/N of many individual spectra, we constructed composite spectra to maximize the use of our full sample and explore the dependence of outflow velocity on galaxy properties through the average absorption line profiles. We focused on the Fe II $\lambda\lambda 2587, 2600\text{\AA}$, Mg II $\lambda\lambda 2796, 2803\text{\AA}$ lines, as well as NaD absorption.

Only galaxies with valid spectral coverage over the region of interest were included in the stacking procedure. For the Fe II and Mg II stacks, we limited the sample to galaxies at $z < 4$ to ensure comparable redshift distributions across all bins. We then divided the sample into bins based on individual galaxy properties. For Fe II and Mg II, we used three bins per property. For M_* , stellar A_V and β , and inclination composites, the bins for Fe II and Mg II contain 46 galaxies. In our sample, 30 galaxies lack at least two detected Balmer lines. Therefore, for the SFR, $E(B - V)$, sSFR, and Σ_{SFR} composites, the number of galaxies in each bin for the Fe II and Mg II

stacks was reduced to 36 galaxies per bin. The properties of the NUV composite spectra are presented in Table 2.

For the NaD composites, before stacking, we removed the stellar continuum contribution from each spectrum by dividing by each galaxy’s best-fit SED as described in Section 3.2.3. We initially constructed composites using the full sample, but the resulting spectra did not yield NaD absorption that was strong enough for reliable line fitting. This is likely due to a combination of low S/N in many individual spectra and dilution of the absorption when stacking spectra that did not show clear NaD detections. To better recover the NaD absorption in the stacks, we limited the NaD composites to galaxies with significant NaD absorption in their individual spectra, yielding a subsample of 32 galaxies. We then divided this subsample into two bins with 16 galaxies each for all NaD composites. The NaD composite properties are listed in Table 3.

To create the composites, we shifted each spectrum to the rest frame and interpolated it onto a common wavelength grid. We normalized the spectra by scaling them to a common flux level, determined from the median flux within a line-free region, 3100–3150 \AA for Fe II and Mg II and 5920–5940 \AA for NaD. We combined the spectra by taking the median flux at each wavelength. The error spectrum of each composite was calculated by summing the squared individual flux uncertainties at each wavelength, dividing by the number of spectra contributing to that wavelength, and taking the square root.

4. RESULTS

In this section, we examine how velocity offsets correlate with galaxy properties. This work builds on our previous analysis (Kehoe et al. 2025), which used only the AURORA survey, by combining the sample with the LyC22 and EXCELS surveys, significantly increasing the number of galaxies to be analyzed. This expanded dataset allows for a more robust investigation of trends between outflow kinematics and galaxy properties, as well as a direct comparison across multiple tracers, including Fe II, Mg II, and NaD. In addition to outflow velocity trends, we examine subsamples of galaxies exhibiting inflows and Mg II emission to explore how these populations differ from the overall sample.

4.1. Correlations with Galaxy Properties

Analyzing correlations between outflow velocity and galaxy properties provides insight into the physical processes that drive galactic outflows. We explore how outflow velocities relate to stellar and dust properties, as well as galaxy inclination. Stellar properties, including

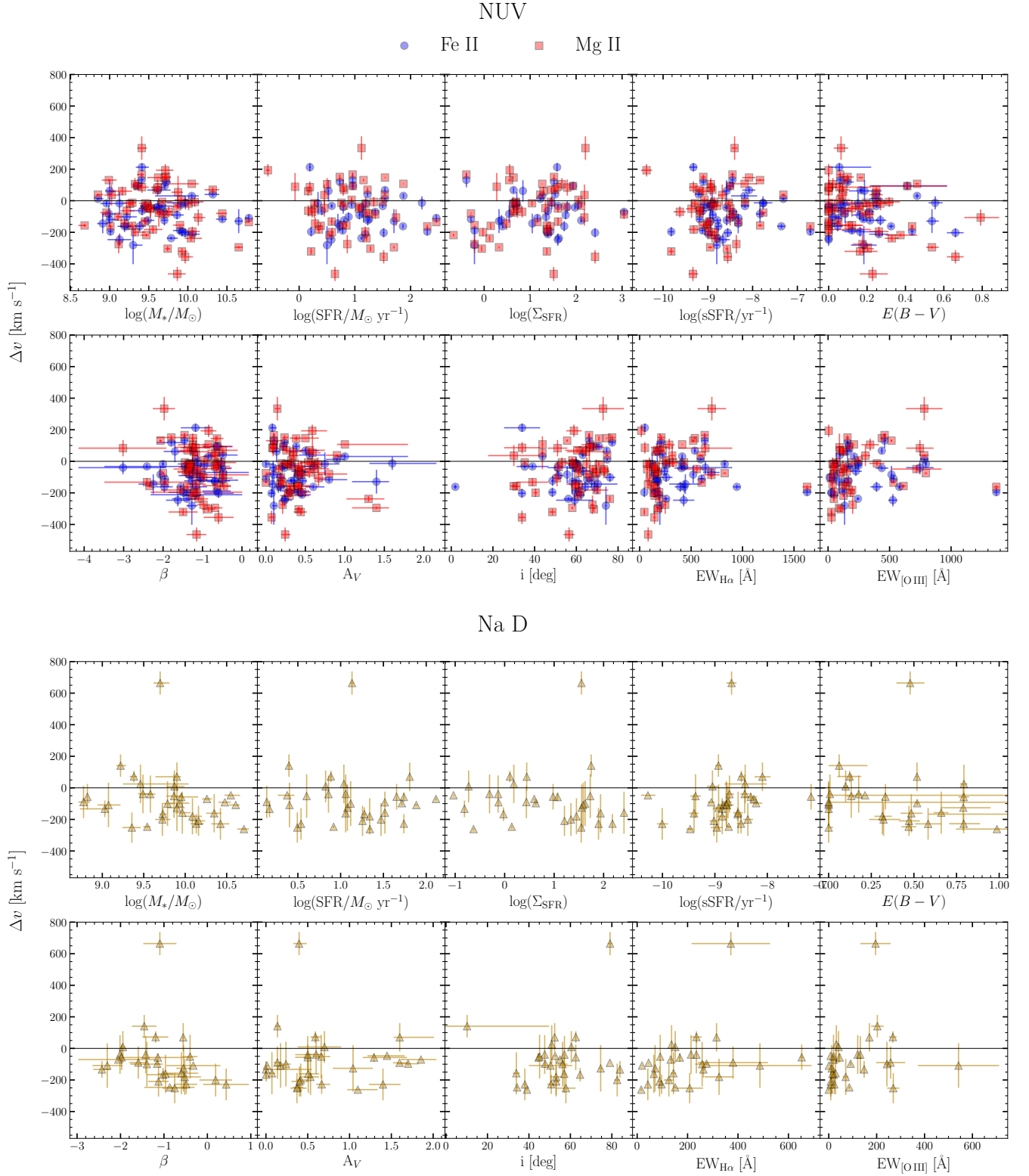


Figure 5. Gas kinematics traced by NUV absorption lines (top; Fe II, blue circles and Mg II, red squares), and optical absorption line (bottom; Na D, gold triangles) absorption line centroids versus galaxy properties. These individual measurements show no correlation between outflow velocity and any galaxy property.

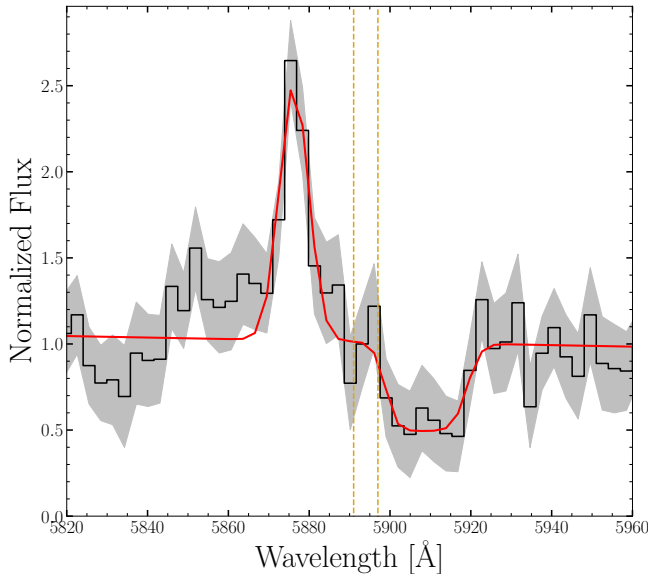


Figure 6. Spectrum in the NaD region for SSA22-20013 from the LyC22 survey at $z = 3.0495$. The best-fitting model is shown in red, and the vertical dashed orange lines mark the rest wavelengths of the NaD $\lambda\lambda 5891, 5897$ absorption doublet. The absorption feature is clearly redshifted relative to the expected rest-frame wavelengths, consistent with the large positive velocity offset identified in Figure 5.

M_* , SFR, sSFR, and Σ_{SFR} , trace the overall growth, star formation activity, and energetic output of galaxies. In addition to these stellar properties, we included the rest-frame EW of [O III] and H α emission lines as indirect tracers of the specific star-formation rate. Dust properties including nebular $E(B - V)$, and stellar A_V and β (though β also reflects the underlying stellar population and nebular continuum), describe the amount and distribution of dust, which have been shown to correlate with the absorption EW of outflowing gas (Du et al. 2021). Correlations with galaxy inclination are sensitive to the geometry of the outflow.

Outflow velocities from individual galaxies, measured using Fe II, Mg II, and NaD absorption lines, are compared against these galaxy properties in Figure 5. One notable outlier is present in the NaD measurements, where a single galaxy (SSA22-20013; $z = 3.0495$) exhibits a significantly redshifted absorption velocity traced by the line centroids of $+664 \text{ km s}^{-1}$. This inflow velocity is greater in magnitude than others recently reported for $z \geq 2$ galaxies (Weldon et al. 2023; Davies et al. 2024). We inspected this spectrum in detail (shown in Figure 6) and confirm that the absorption signal is robust and not the result of noise or an unreliable fit. A detailed analysis of this source is warranted, but outside the scope the current work.

We tested for correlations using the Spearman rank coefficient and found no significant trend between gas kinematics and any galaxy property. For each tracer, we also separated the sample into galaxies with and without significant outflow detections. Significant outflow detections are defined as $|\Delta v| > \sigma_{\Delta v}$, where $\sigma_{\Delta v}$ is the uncertainty on the velocity measurement, and $\Delta v < 0$. The non-outflow sample includes both galaxies without line detections and galaxies where $|\Delta v| \leq \sigma_{\Delta v}$. Using the KS test to assess whether these two populations come from the same parent distribution (Figure 7), we found that galaxies with detected outflows in any tracer had statistically higher masses. Galaxies with Fe II outflows also showed higher SFR, Σ_{SFR} , and H α EW and galaxies with outflows detected from NaD also had higher SFR, nebular $E(B - V)$, stellar A_V and β , and lower [O III] EW and inclination (i.e., more face-on).

We also analyzed composite spectra to probe the average outflow properties across bins of galaxy parameters. These stacked profiles reveal how outflow velocities and absorption strengths vary with stellar, dust, and geometric properties, providing complementary measurements from individual galaxy spectra. In Figures 8 and 9 we compare the composite spectra for Fe II and Mg II across the different galaxy properties.¹ To quantify outflow velocities, we used v_{80} , defined as the velocity where the absorption reaches 80% of the continuum on the blue side of the profile. We used v_{80} instead of centroid measurements because resonant emission can partially fill in absorption features, biasing centroids towards larger blueshifts (Prochaska et al. 2011; Erb et al. 2012; Martin et al. 2012; Kornei et al. 2013).

We measured v_{80} by identifying the absorption minimum and stepping toward bluer wavelengths until the sum of the flux and its uncertainty exceeded 0.8 of the continuum. Uncertainties were estimated by perturbing

¹ Although not the focus of the current study, we note that Fe II* $\lambda 2612$ and $\lambda 2626$ fine-structure emission is not detected in the composite spectra shown in Figures 8 and 9. The lack of detected Fe II* emission stands in contrast to the fine-structure emission observed by, e.g., Kornei et al. (2013) and Erb et al. (2012) in star-forming galaxies at $z \sim 1 - 2$. Fe II* emission is also absent in local starburst galaxy spectra (Leitherer et al. 2011), which is explained by Gialalisco et al. (2011) as being due to slit-losses. Accordingly, the physical size subtended by the $z \sim 0$ slit observations ($\sim 100 \text{ pc}$) may not encompass a more extended Fe II*-emitting halo. Likewise, the small ($0.2''$) NIRSpec slit may also miss Fe II* emission if it originates in an extended ($> \text{few-kpc-scale}$) distribution.

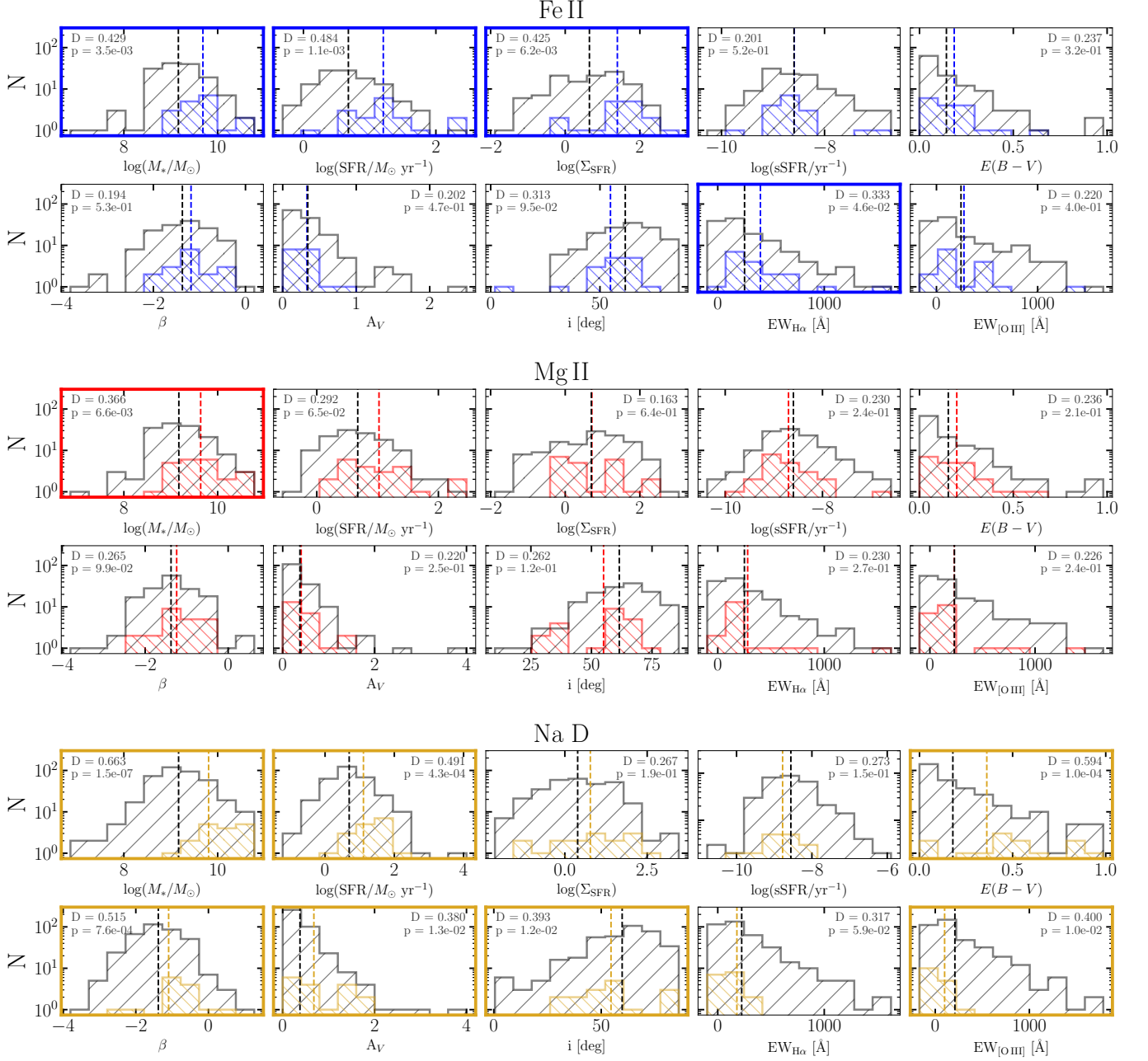


Figure 7. Distributions of galaxy properties for those with significant Fe II (top; blue), Mg II (middle; red), and Na D (bottom; gold) outflow detections ($\Delta v < 0$ and $|\Delta v| > \sigma_{\Delta v}$) and galaxies with no outflow detections (gray). Vertical dashed lines indicate mean values for each sample. The KS D statistic and p -values are reported in the upper corners of each panel. Significant results are highlighted in blue (Fe II), red (Mg II), and gold (Na D). Galaxies with Fe II, Mg II and Na D outflows exhibit significantly higher M_* , galaxies with Fe II outflows have significantly higher SFR and Σ_{SFR} , and galaxies with Na D outflows have significantly higher SFR, nebular $E(B - V)$, and stellar A_V and β , and lower inclination compared to those without detected outflows.

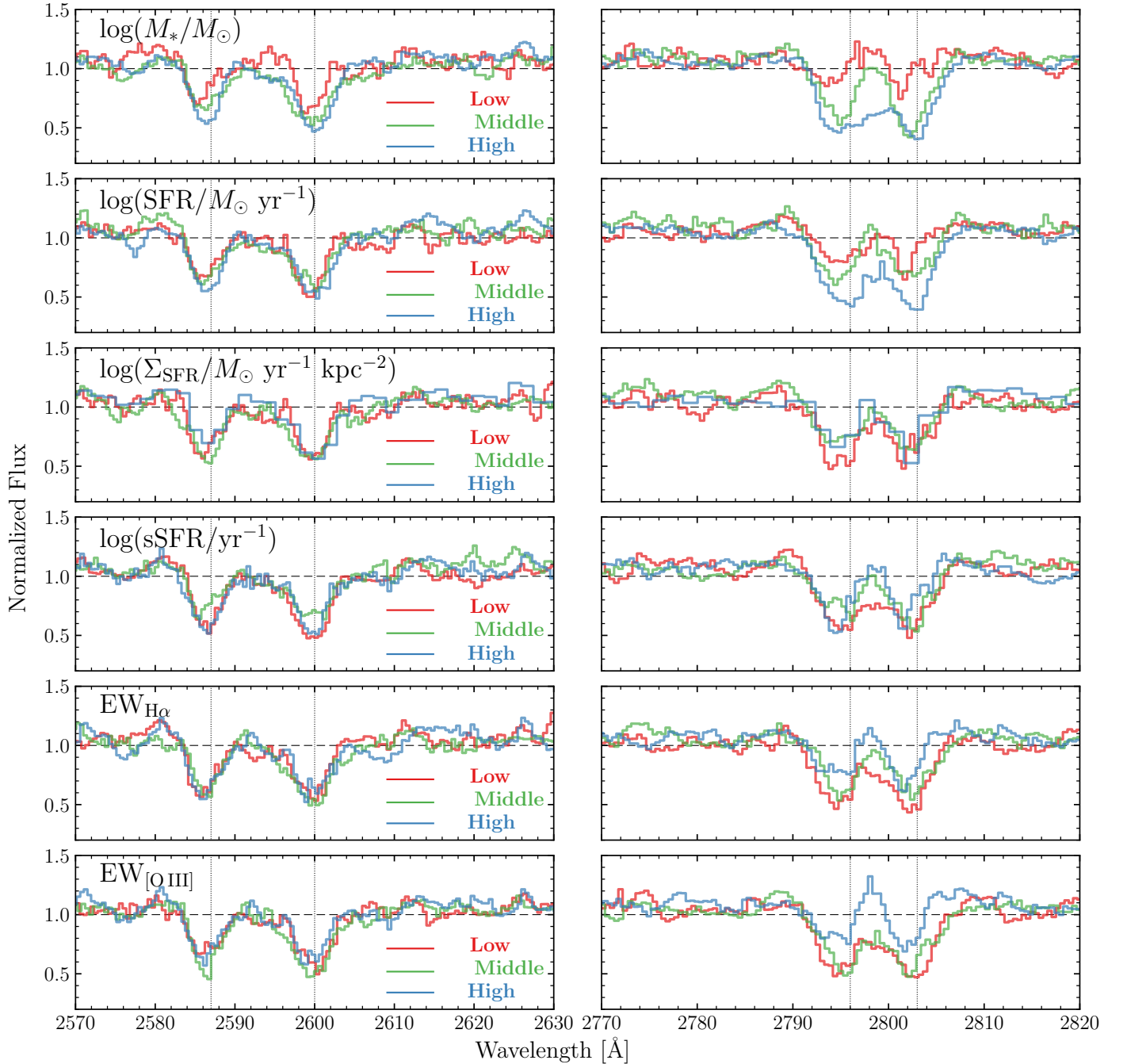


Figure 8. Composite spectra of galaxies binned by stellar properties, with Low, Middle, and High bins shown in red, green, and blue, respectively. The left panels show Fe II $\lambda 2587$ and $\lambda 2600$, while the right panels show the Mg II $\lambda \lambda 2796, 2803$ doublet. Vertical dashed lines indicate the rest wavelengths of the absorption features. Emission filling is most evident in Mg II profiles, particularly for stellar mass, SFR and [O III] EW.

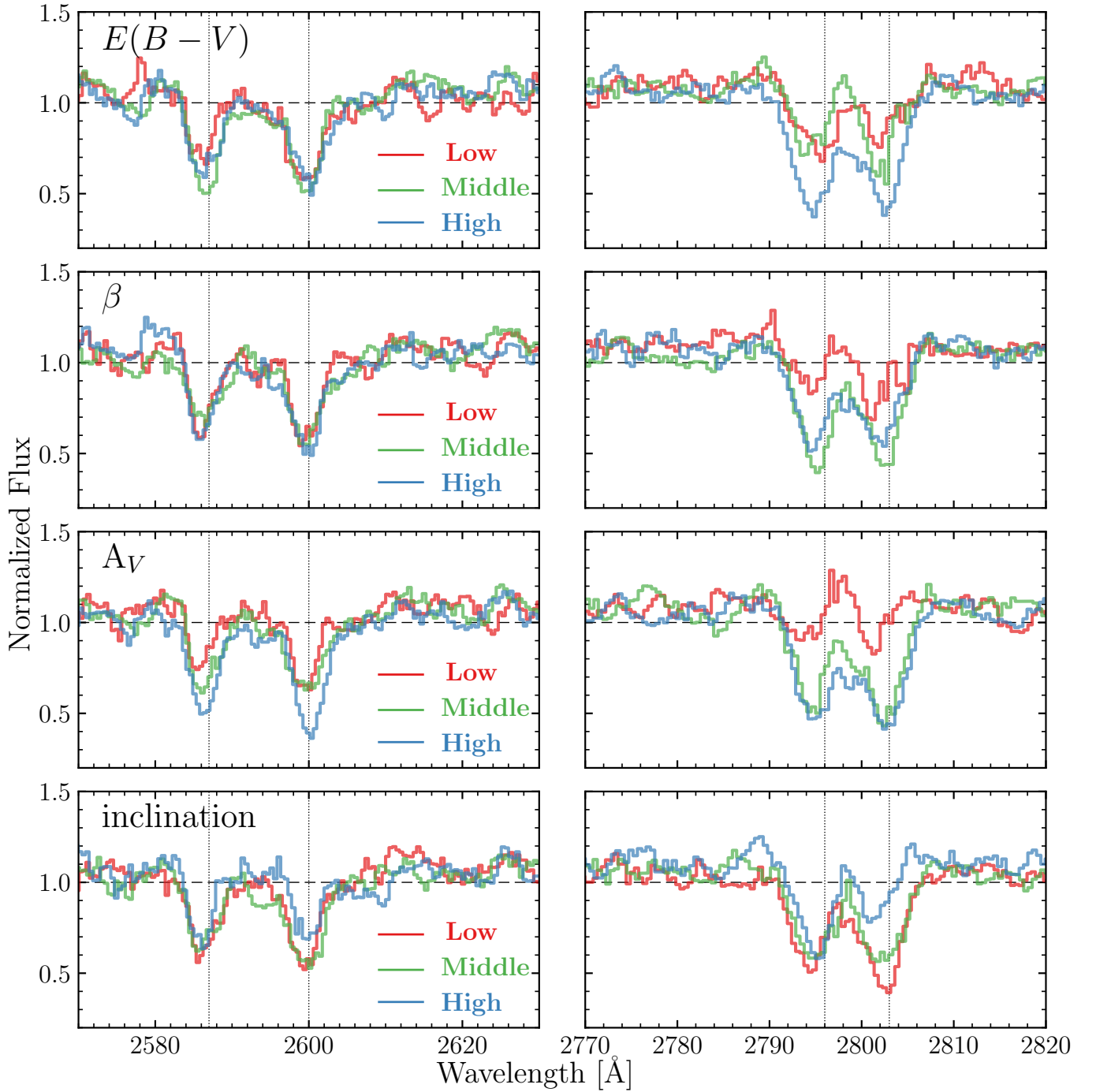


Figure 9. Same as Figure 8, but for galaxies binned by dust properties and inclination. Low, Middle, and High bins are shown in red, green, and blue, respectively. Emission filling is most pronounced in the Mg II profiles for nebular $E(B - V)$, and stellar A_V and β .

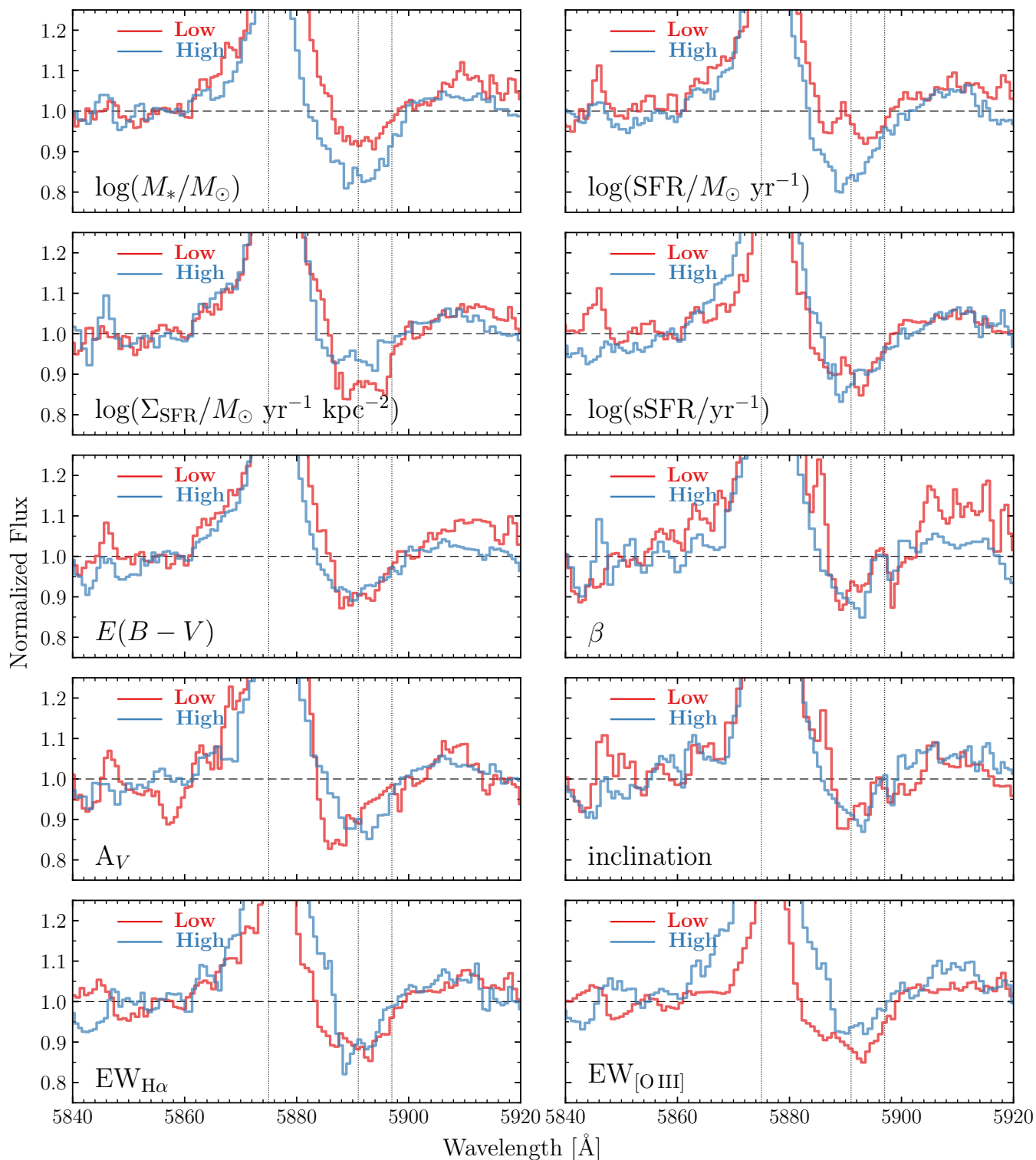


Figure 10. Continuum-divided composite spectra of galaxies for Na D $\lambda\lambda 5891, 5897$ with He I $\lambda 5875$ emission, binned by galaxy properties. Low and High bins are shown in red and blue, respectively. Vertical dashed lines indicate the rest wavelengths of the line features.

Table 2. Composite Spectra Measurements for Fe II and Mg II

Property	Composite	N^a	$N_{\text{Mg II,em}}^b$	S/N	Average Property Value	$v_{80, \text{Fe II}}^c$	$v_{80, \text{Mg II}}^c$	$\text{EW}_{\text{Fe II}}^d$	$\text{EW}_{\text{Mg II}}^d$
				[pixel ⁻¹]	and Range	[km s ⁻¹]	[km s ⁻¹]	[Å]	[Å]
$\log(M_*)$	Low	46	7	15	8.85 (8.43–9.08)	-215 ± 51	-325 ± 259	0.9 ± 0.2	2.6 ± 0.2
	Middle	46	2	26	9.30 (9.10–9.49)	-347 ± 32	-398 ± 14	4.5 ± 0.1	4.0 ± 0.1
	High	46	2	14	9.86 (9.50–10.78)	-278 ± 32	-442 ± 20	6.5 ± 0.2	4.8 ± 0.2
$\log(\text{SFR})$	Low	36	2	20	0.22 ((-0.31)–0.49)	-274 ± 39	-213 ± 91	2.1 ± 0.2	3.4 ± 0.2
	Middle	36	4	33	0.66 (0.49–0.87)	-241 ± 50	-388 ± 56	3.7 ± 0.1	4.0 ± 0.2
	High	36	4	15	1.30 (0.88–2.46)	-266 ± 37	-443 ± 26	6.5 ± 0.2	4.7 ± 0.2
$\log(\text{sSFR})$	Low	36	1	30	-9.26 ((-10.28)–(-8.95))	-312 ± 22	-438 ± 33	5.0 ± 0.1	4.1 ± 0.1
	Middle	36	5	24	-8.81 ((-8.95)–(-8.59))	-259 ± 27	-170 ± 61	3.7 ± 0.1	3.8 ± 0.1
	High	36	4	13	-8.22 ((-8.58)–(-7.23))	-256 ± 36	-357 ± 27	2.9 ± 0.2	4.5 ± 0.2
$\log(\Sigma_{\text{SFR}})$	Low	36	3	17	-0.03 ((-1.03)–0.54)	-250 ± 43	-396 ± 22	4.6 ± 0.2	3.5 ± 0.2
	Middle	36	4	12	1.14 (0.60–1.39)	-195 ± 60	-259 ± 146	3.8 ± 0.2	4.6 ± 0.2
	High	36	4	38	1.82 (1.39–3.04)	-319 ± 35	-423 ± 83	3.3 ± 0.1	3.7 ± 0.1
$E(B - V)$	Low	36	3	24	0.004 (0.00–0.03)	-338 ± 37	-196 ± 51	2.8 ± 0.1	3.6 ± 0.2
	Middle	36	6	12	0.09 (0.03 – 0.16)	-253 ± 41	-292 ± 121	2.8 ± 0.2	4.4 ± 0.2
	High	36	1	24	0.32 (0.16–0.98)	-254 ± 47	-495 ± 27	6.4 ± 0.1	4.3 ± 0.2
A_V	Low	46	6	12	0.12 (0.00–0.19)	-189 ± 56	-247 ± 348	0.7 ± 0.2	2.8 ± 0.2
	Middle	46	4	17	0.28 (0.20–0.40)	-247 ± 48	-392 ± 28	5.1 ± 0.1	3.8 ± 0.2
	High	46	1	27	0.63 (0.40–1.64)	-296 ± 22	-437 ± 21	6.0 ± 0.1	5.0 ± 0.1
β	Low	46	8	13	-1.82 ((-3.02)–(-1.46))	-248 ± 42	-157 ± 165	2 ± 0.2	3.3 ± 0.2
	Middle	46	1	26	-1.21 ((-1.46)–(-1.06))	-313 ± 32	-428 ± 15	5.4 ± 0.1	4.2 ± 0.1
	High	46	2	21	-0.60 ((-1.05)–0.20)	-281 ± 23	-426 ± 32	4.8 ± 0.1	4.0 ± 0.1
inclination	Low	46	4	23	46 (2–58)	-225.3 ± 32	-466 ± 245	5.3 ± 0.1	4.4 ± 0.1
	Middle	46	2	26	63 (58–68)	-241 ± 42	-423 ± 34	4.9 ± 0.1	4.2 ± 0.1
	High	46	5	15	76 (68–86)	-88 ± 51	-323 ± 38	2.9 ± 0.1	2.3 ± 0.2
$\text{EW}_{\text{H}\alpha}$	Low	41	1	25	116 (38–170)	-225 ± 45	-516 ± 28	3.7 ± 0.2	5.2 ± 0.1
	Middle	41	1	20	232 (170–343)	-230 ± 34	-411 ± 197	4.6 ± 0.2	4.3 ± 0.1
	High	41	7	12	644 (365–1530)	-135 ± 55	-138 ± 56	3.8 ± 0.2	4.0 ± 0.2
$\text{EW}_{[\text{O III}]}$	Low	41	0	27	72 (4–128)	-215 ± 56	-451 ± 23	3.8 ± 0.1	5.6 ± 0.1
	Middle	41	1	26	181 (130–261)	-277 ± 35	-380 ± 242	4.8 ± 0.1	5.3 ± 0.1
	High	41	8	12	680 (269–1648)	-106 ± 52	-127 ± 116	3.6 ± 0.2	1.6 ± 0.2

^aNumber of galaxies included in each composite spectrum.

^bNumber of Mg II emitters (Section 4.3) included in each composite spectrum.

^c v_{80} is defined as the velocity where the absorption reaches 80% of the continuum on the blue side of the profile.

^dRest-frame absorption equivalent width.

the spectra according to their error spectra and repeating the measurement 1000 times. For the Fe II and Mg II composites, the blue wings of the absorption profiles are consistent across most properties (Figures 8, 9, Table 2), yielding comparable velocities within the uncertainties. The lack of strong monotonic trends suggests that any correlations in outflow kinematics are either weak or obscured by measurement uncertainties and spectral

resolution. We find a significant correlation between v_{80} and inclination, where v_{80} increases in magnitude (more blueshifted) at smaller inclination (i.e., more face-on), suggesting that outflows may be collimated (Bordoloi et al. 2011; Kornei et al. 2012) and that true outflow velocities may be underestimated in many cases because we are observing projected velocities. A more detailed discussion of this trend is presented in Section 5.2.

Table 3. Composite Spectra Measurements for Na D

Property	Composite	N ^a	S/N	Average Property Value	Δv_{NaD}^b	EW _{NaD} ^c
			[pixel ⁻¹]	and Range	[km s ⁻¹]	[Å]
log(M_*)	Low	16	26	9.4 (8.77–9.87)	-77 ± 37	2.4 ± 0.2
	High	16	59	10.2 (9.87–10.71)	-142 ± 9	2.6 ± 0.1
log(SFR)	Low	16	27	0.68 (0.13–1.08)	-101 ± 41	2.1 ± 0.2
	High	16	49	1.53 (1.12–2.11)	-140 ± 11	2.7 ± 0.1
log(sSFR)	Low	16	37	$-9.16 ((-10.8)-(-8.78))$	-142 ± 13	2.1 ± 0.2
	High	16	30	$-8.08 ((-8.75)-(-7.17))$	-92 ± 20	2.5 ± 0.1
log(Σ_{SFR})	Low	16	34	$-0.02 ((-1.03)-0.98)$	-95 ± 11	2.7 ± 0.1
	High	16	30	1.65 (1.07–2.41)	-126 ± 26	2.0 ± 0.2
$E(B - V)$	Low	16	27	0.14 (0.00–0.47)	-115 ± 18	2.5 ± 0.2
	High	16	47	0.82 (0.47–1.55)	-134 ± 16	2.2 ± 0.2
A_V	Low	16	25	0.27 (0.00–0.51)	-137 ± 17	2.2 ± 0.2
	High	16	58	1.27 (0.53–3.6)	-120 ± 15	2.7 ± 0.1
β	Low	16	27	$-1.66 ((-2.42)-(-1.13))$	-65 ± 17	2.6 ± 0.1
	High	16	34	$-0.54 ((-1.09)-0.43)$	-139 ± 16	1.8 ± 0.2
inclination	Low	16	41	11 (10–53)	-129 ± 20	2.2 ± 0.1
	High	16	33	313 (53–84)	-133 ± 13	2.3 ± 0.1
EW _{Hα}	Low	16	56	98 (16–151)	-147 ± 7	2.2 ± 0.1
	High	16	23	343 (169–652)	-88 ± 23	2.5 ± 0.2
EW _[O III]	Low	16	56	19 (0–45)	-149 ± 5	2.0 ± 0.1
	High	16	22	200 (71–542)	-39 ± 44	2.4 ± 0.2

^aNumber of galaxies included in each composite spectrum.

^bCentroid velocity offset for Na D.

^cRest-frame absorption equivalent width.

For Na D, we compare the composites of the two bins in Figure 10 and Table 3. The Na D composites are based on a smaller subsample than the Fe II and Mg II stacks, since we only include galaxies with individual Na D detections. We adopted centroid velocities rather than v_{80} because the nearby He I emission line contaminates the blue wing of the Na D absorption profile. The centroid therefore provides a more stable estimate of the absorption kinematics for Na D. A clear trend is seen with M_* and H α and [O III] EW, where galaxies with higher M_* and lower emission-line EWs exhibit more blueshifted absorption (Table 3). A possible correlation is also seen with β , with redder (more positive β) galaxies exhibiting more blueshifted Na D absorption, although the significance of this trend is unclear given the lack of similar trends in other dust properties. Unlike the NUV tracers, the inclination bins in the Na D composites show consistent velocities within the uncertainties, indicating no

strong geometric dependence, though selection effects in the Na D sample may obscure subtler underlying trends.

Fe II, Mg II, and Na D absorption EWs provide an additional probe of the absorbing gas and trace the column density and the amount of outflowing material. We therefore examine how these EWs vary with galaxies properties for both the NUV tracers and Na D (Figure 11). For the Fe II and Mg II transitions, the EWs show clear trends with increasing M_* , SFR, nebular $E(B - V)$, stellar A_V , and decreasing inclination. For Na D EW, there are similar trends with increasing M_* and SFR. However, the dust related trends are less uniform, with A_V showing a positive correlation with EW, while β shows the opposite. This inconsistency is likely due to the composite sample not being fully representative of the parent sample. The galaxies contributing to the Na D stacks are biased toward more massive, higher SFR, and dustier systems, which shifts the effective dust properties in the composites. Recovering the trends in the composites will require a larger and higher S/N data

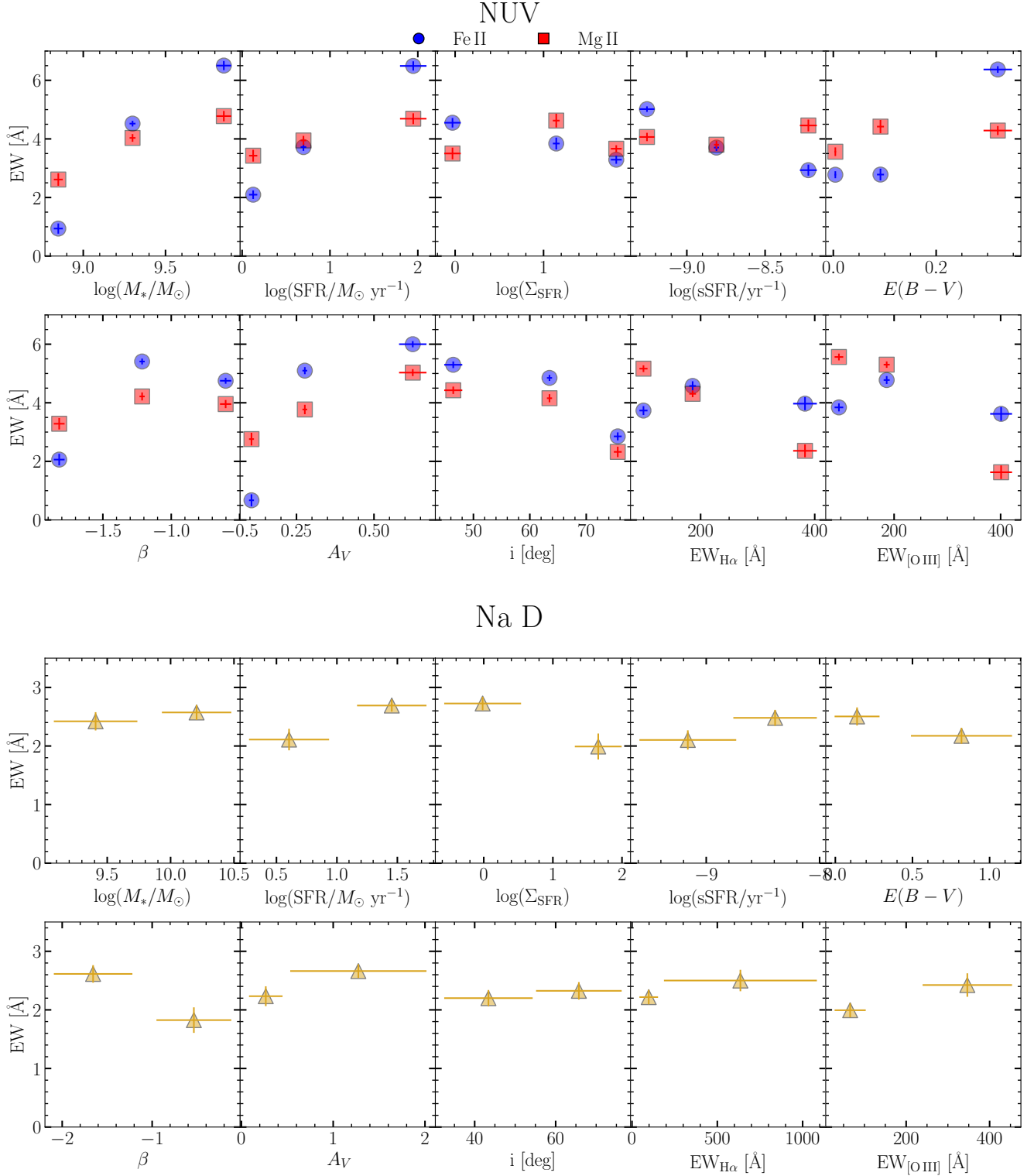


Figure 11. EWs of NUV absorption lines (top) (i.e. Fe II λ 2587, λ 2600, summed over both lines (blue), and Mg II λ 2796, 2803 (red)) and the Na D λ 5891, 5897 doublet (bottom; gold) measured from the composite spectra binned by galaxy properties. For the NUV lines, the EW increases with stellar mass, SFR, A_V , and decreases with galaxy inclination. For Na D, the EW increases with SFR, and sSFR, and A_V , and decreases with Σ_{SFR} , and β .

in the NaD region to reliably recover the doublet in stacked spectra using the full sample. We discuss the relationship between outflow velocity and strength and galaxy properties further in Section 5.1.

4.2. Galaxy Inflows

Gas inflows are a fundamental component of galaxy evolution as they replenish the supply of cold gas within galaxies. Observations have shown that, without continued gas accretion, the existing cold gas reservoirs would be depleted on relatively short timescales, preventing galaxies from sustaining their SFRs (Kennicutt 1989; Prochaska & Wolfe 2009; Bauermeister et al. 2010; Leroy et al. 2008; Saintonge et al. 2017; Tacconi et al. 2018). Gas accretion is commonly identified through inflow signatures, such as redshifted absorption features relative to the systemic velocity (Rubin et al. 2012; Calabrò et al. 2022; Weldon et al. 2023; Bevacqua et al. 2026). However, such signatures are difficult to detect, as they can be weak, have low covering fractions, are metal-poor, and are often sensitive to the viewing geometry (Steidel et al. 2010; Faucher-Giguère & Kereš 2011; Fumagalli et al. 2011; Kimm et al. 2011; Péroux et al. 2020).

Defining a subsample of galaxies that exhibit inflow signatures allows us to directly examine how gas accretion relates to various galaxy properties, helping constrain the physical conditions under which inflows occur. Applying our inflow selection criteria ($\Delta v > 0$ and $|\Delta v| > \sigma$), we identify a subsample of 15 galaxies with evidence for inflows. Of these 15 inflows, 1 is traced by Fe II, 8 are traced by Mg II, 4 are traced by both Fe II and Mg II, and 2 are traced by Na D. In all three tracers, inclination is the only galaxy property for which we observe a clear trend in inflow incidence. Combining the inflow detections from all tracers and comparing them to galaxies without detected inflows, we find a statistically significant difference in their inclination ($p \approx 0.03$), corresponding to a $>2\sigma$ significance level. We find that inflows are preferentially detected in higher inclination (more edge-on) galaxies (Figure 12), suggesting that viewing geometry plays an important role in our ability to detect accreting gas. We return to the interpretation of this trend in Section 5.3.

4.3. Mg II Emitters

A subset of galaxies in our sample exhibit significant Mg II emission. The Mg II line profiles can vary from strong absorption to emission-dominated, reflecting the resonant nature of the transition. In this process, absorbed photons are re-emitted and scattered by outflowing gas, producing emission near the systemic velocity and modifying the overall profile shape (Weiner et al.

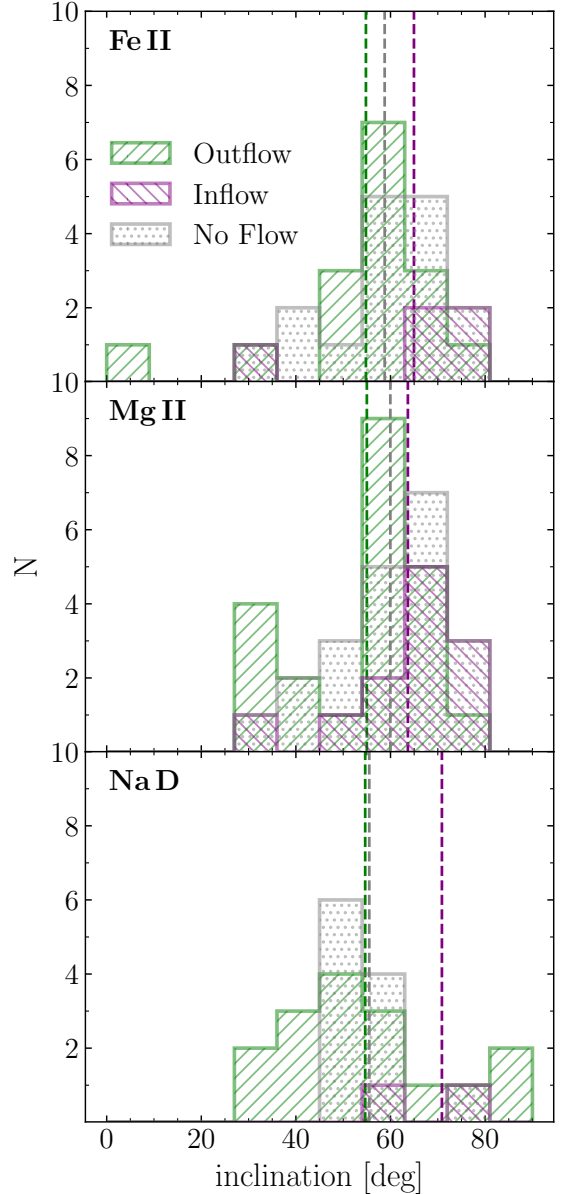


Figure 12. Histograms of galaxy inclinations for Fe II (top), Mg II (middle), and Na D (bottom). Galaxies with detected outflows (green; $\Delta v < 0$ and $|\Delta v| > \sigma_{\Delta v}$), inflows (purple; $\Delta v > 0$ and $|\Delta v| > \sigma_{\Delta v}$), and no significant flows (gray; absorption fitting but $|\Delta v| \leq \sigma_{\Delta v}$) are shown. Vertical lines indicate the average inclination for each subsample. In all tracers, inflows are more commonly found in higher inclination (more edge-on) galaxies.

2009; Rubin et al. 2010; Martin et al. 2013; Prochaska et al. 2011; Henry et al. 2018; Chisholm et al. 2020; Xu et al. 2023).

Detection rates of Mg II emission reported in the literature span a broad range (~ 1 –70%) at similar redshifts, driven primarily by difference in the properties of the galaxy samples and identification methods and the

quality of data (Weiner et al. 2009; Rubin et al. 2010; Erb et al. 2012; Guseva et al. 2013; Feltre et al. 2018). Methods based on flux excess redward of the Mg II transitions tend to be more conservative (Weiner et al. 2009; Rubin et al. 2010), while pixel-based (Erb et al. 2012) or EW criteria are more sensitive to weaker emission features (Kornei et al. 2012; Feltre et al. 2018).

To maintain consistency with our previous analysis (Kehoe et al. 2025), we adopt the same conservative selection method based on detecting flux above the continuum redward of the Mg II lines (Weiner et al. 2009; Rubin et al. 2010). This approach isolates the strongest Mg II emitters in our sample. We find 14 galaxies have strong Mg II emission, corresponding to 8% of galaxies with Mg II spectral coverage. In Figure 13, we compare these “Mg II emitters” to galaxies without significant Mg II emission, restricting the comparison to objects with $S/N > 3$ in the region surrounding the Mg II profile to minimize biases from low-quality spectra. Applying a KS test, we find that Mg II emitters have lower stellar masses and bluer β , and higher sSFRs relative to galaxies without significant Mg II emission. The connection between Mg II emission and galaxy properties is explored in more detail in Section 5.4.

We also examine the contribution of Mg II emitters in the composite spectra binned by galaxy properties (Figure 8 and Figure 9). Emission filling is visible in the Mg II profiles across several bins, particularly where the underlying absorption is weaker, such as in the low stellar mass, low $E(B - V)$, low (more negative) β , and low A_V bins. In these composites, the emission partially fills in the absorption features, illustrating how even a small number of strong emitters (Table 2) can influence the average line profiles.

5. DISCUSSION

5.1. Comparison to Other Outflow Studies

5.1.1. NUV Absorption

Fe II and Mg II trace low-ionization gas associated with cool, partially ionized material in galaxies. While we find no significant correlations between NUV outflow velocities and any galaxy property, we do find that galaxies with detected NUV outflows are biased toward higher M_* , SFR and Σ_{SFR} (Figure 7). These trends are consistent with our previous analysis using only the AURORA survey (Kehoe et al. 2025) and are in agreement with other observations as we discuss below.

Outflow velocities traced by NUV absorption at $z \sim 1$ have been shown to increase with SFR and Σ_{SFR} (Martin et al. 2012; Kornei et al. 2012; Bradshaw et al. 2013; Bordoloi et al. 2014; Heckman et al. 2015; Heckman & Borthakur 2016; Prusinski et al. 2021; Xu et al. 2022).

In particular, when analyzing NUV observations of 1400 galaxies at $z \sim 1.4$ Weiner et al. (2009) found a scaling relation $v_{10\%} \propto \text{SFR}^{0.3}$. Here, $v_{10\%}$ is where the absorption reaches 90% of the continuum on the blue side of the profile. Other studies, however, have found no significant correlation (Steidel et al. 2010; Talia et al. 2012; Calabrò et al. 2022), due to a limited dynamic range, with SFRs spanning only 10–100 $M_\odot \text{ yr}^{-1}$. In our previous analysis (Kehoe et al. 2025), we found no correlation as the sample spans a comparably narrow dynamic range. Similarly, with our expanded sample, we did not observe a clear dependence of outflow velocity on SFR as our v_{80} values in the low- and high-SFR composites are consistent within the uncertainties (Table 2). A clear correlation between outflow velocity and SFR generally requires including galaxies with much lower SFRs of $\text{SFR} < 1 M_\odot \text{ yr}^{-1}$ (Martin 2005; Xu et al. 2022). While our expanded sample includes more galaxies in this low-SFR regime, a larger number of low-SFR galaxies is still needed to find a significant correlation with either the composites or individual measurements. However, we observed that galaxies with detected outflows are preferentially detected in systems with higher SFR and Σ_{SFR} (Figure 7), which is broadly consistent with the picture in which strong star formation activity is associated with galactic outflows.

Trends with M_* in NUV observations are also variable across samples, with some studies reporting positive correlations ($v_{10\%} \propto M_*^{0.17}$) (Weiner et al. 2009; Rubin et al. 2010; Erb et al. 2012) and others finding no dependence (Martin et al. 2012; Bordoloi et al. 2011; Prusinski et al. 2021). This difference can also be explained by a narrow dynamic range, as shown by Prusinski et al. (2021), with masses $9.3 \leq \log(M/M_\odot) \leq 10.8$. We do not observe a clear correlation with mass as the lowest bins have large uncertainties and the middle and high bins show comparable blueshifts (Table 2). Although our sample spans a larger mass range, the lack of a robust trend may be due to a combination of selection effects, observational uncertainties, and differences in galaxy properties such as SFR, gas content, and outflow geometry that can influence measured outflow velocities (Bordoloi et al. 2011; Martin et al. 2012; Prusinski et al. 2021). Consistent with previously reported trends (Weiner et al. 2009; Rubin et al. 2010; Erb et al. 2012), we found that galaxies with detected outflows are biased toward higher stellar masses (Figure 7), suggesting that while a clear scaling relation is not evident in our NUV sample, outflow incidence may still increase with mass.

We also found that the EW of absorption lines increases with M_* , SFR, nebular $E(B - V)$, and stellar A_V (Figure 11), suggesting that the variations in the NUV

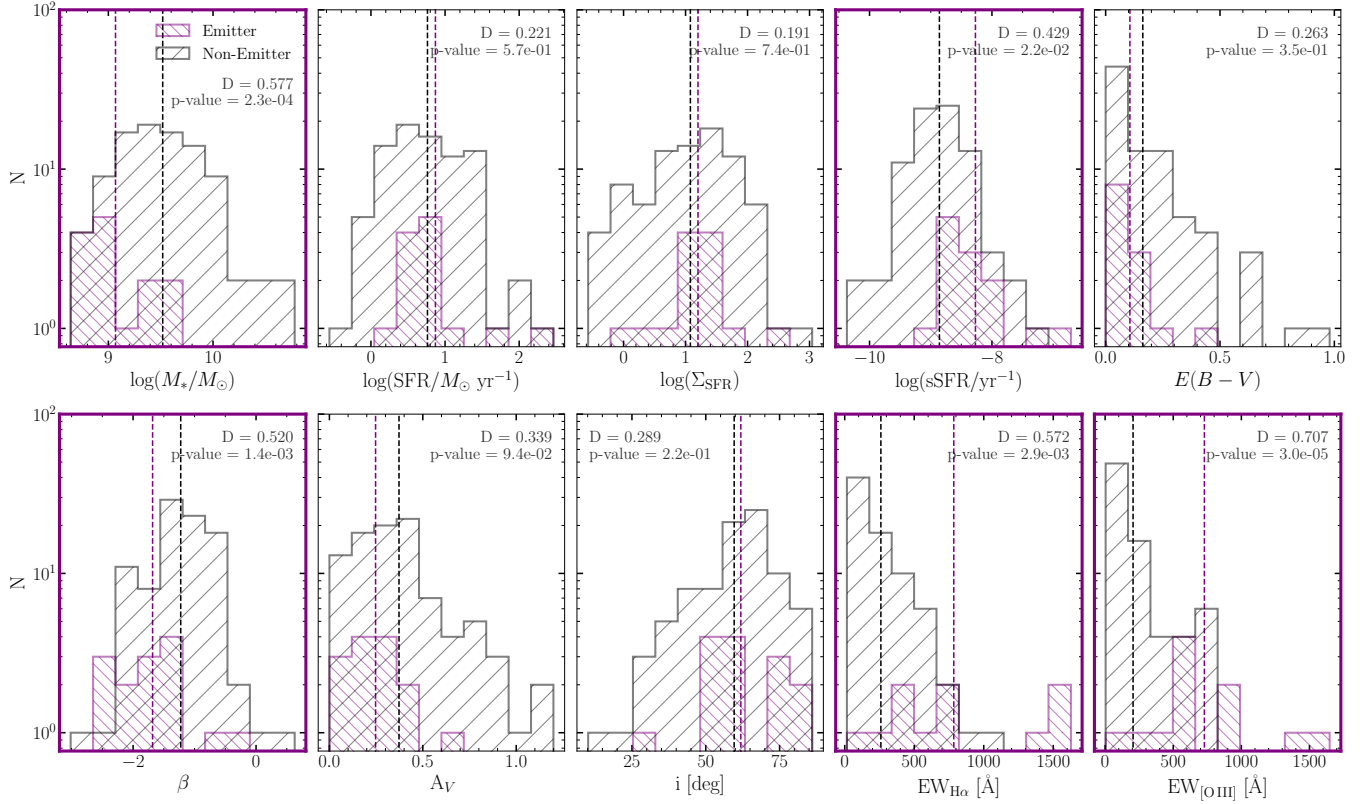


Figure 13. Histograms showing the distributions of various galaxy properties for the Mg II non-emitter (gray) and Mg II emitter (purple) samples. Dashed gray and purple lines indicate the average values for non-emitters and emitters, respectively. The KS D statistic and p -values are reported in the upper corners of each panel. Figures with significant results are highlighted in bold purple. On average, Mg II emitters have lower stellar mass and β , and higher sSFR and H α and [O III] emission EW than non-emitters.

absorption strength may be driven by changes in the column density and covering fraction of low-ionization gas rather than outflow velocity. Similar correlations between Fe II and Mg II absorption EWs and galaxy properties have been widely reported in $z \sim 1$ samples (Weiner et al. 2009; Rubin et al. 2010; Rubin et al. 2014; Martin et al. 2012; Bordoloi et al. 2014; Prusinski et al. 2021). As these transitions are optically thick, the absorption EW is largely governed by the covering fraction and velocity dispersion of the absorbing material, while also being sensitive to the coupling between dust and metal-enriched neutral gas, where higher dust content is associated with strong low-ionization absorption (Du et al. 2021). This trend may also be influenced by emission line filling, as discussed in Section 5.4. The observed increase in absorption EW with M_* , SFR, nebular $E(B - V)$, and stellar A_V , and supports a picture in which more massive, actively star-forming, and dust-rich galaxies host outflows that cover a larger fraction of the background continuum and span a wider range of velocities (Reddy et al. 2022).

These results indicate that while outflow velocity does not depend on any galaxy properties in our sample, the

incidence of detected outflows increases with M_* , SFR, and Σ_{SFR} , and the strength of the absorption increases with M_* , SFR, and A_V . These trends are consistent with NUV studies at $z \sim 1$, which probe galaxies at significantly lower redshift than our $z \gtrsim 2.5$ sample, highlighting that similar outflow trends may persist across cosmic time.

5.1.2. Na D Absorption

Na D absorption traces cooler, neutral gas that is often associated with dusty outflowing material (Heckman et al. 2000; Veilleux et al. 2005; Chen et al. 2010; Avery et al. 2022; Davies et al. 2024). We find no significant correlations between Na D outflow velocity and galaxy properties in the individual measurements. However, galaxies with detected Na D outflows tend to have higher M_* , SFR, nebular $E(B - V)$, and stellar A_V and β , and lower [O III] EW, indicating Na D outflows are more easily detected in more massive, actively star-forming, dustier galaxies. The difference between the SFR and emission-line EW trends reflects the fact that the EWs most closely trace the sSFR as opposed to total SFR. These results agree with our previous work based on

only 10 galaxies (Kehoe et al. 2025), now expanded to a total of 32 detections of Na D.

Previous work in the local universe found consistent results, where Na D outflows are found in galaxies with higher masses, SFRs, and dust content (Heckman et al. 2000; Martin 2005; Chen et al. 2010; Avery et al. 2022). *JWST* observations allow for Na D to be observed at much higher redshifts ($z \sim 2$) (Belli et al. 2024; Davies et al. 2024; D’Eugenio et al. 2024; Sun et al. 2025; Moretti et al. 2026). Using 113 galaxies at ($1 \lesssim z \lesssim 3$), Davies et al. (2024) found that Na D outflows are typically detected in more massive galaxies ($\log M_*/M_\odot > 10$), in agreement with our mass trend. These higher redshift studies also suggest that while star formation likely dominates the driving mechanism of neutral outflows in the local Universe, AGN activity at higher redshift may contribute to or enhance Na D outflows (Belli et al. 2024; D’Eugenio et al. 2024; Sun et al. 2025; Taylor et al. 2026).

We find that the composite spectra show a general increase in Na D absorption EW and blueshift with M_* and SFR, and less consistent behavior with sSFR and dust properties. However, these results should be interpreted with caution. The composites only include galaxies with significant individual Na D detections and are therefore biased toward higher M_* , SFR, nebular $E(B - V)$, and stellar A_V and β , and lower [O III] EW relative to the full sample. After continuum normalizing the spectra by dividing by the best-fit stellar continuum from SED fitting, the residual Na D absorption is significantly reduced, indicating that the outflow component is weak and difficult to isolate in the stacked spectra. A larger, higher signal-to-noise sample is required to robustly isolate the outflowing component of Na D absorption in composite spectra and better quantify its dependence on the global properties of star-forming galaxies at high redshift.

5.2. Geometry of Outflowing Gas

The outflow kinematics of the composite spectra exhibit a clear dependence on inclination. As shown in Figure 14, the lower inclination (more face-on) composites have higher Fe II and Mg II absorption EWs and higher maximum outflow velocities compared to the higher inclination (more edge-on) bins. The Low- and High-inclination bins differ in v_{80} by 2.3σ for Fe II and 3.2σ for Mg II. This trend indicates that the outflow signal is stronger when galaxies are viewed more face-on, suggesting that the outflowing material is not isotropic. Instead, the inclination dependence points to a more structured outflow geometry, where the detectability

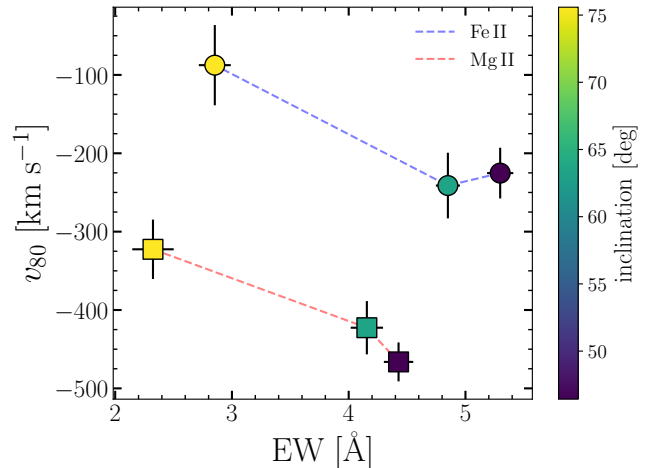


Figure 14. v_{80} vs. EW from the composite spectra for Fe II (circles) and Mg II (squares) absorption. Points are color-coded by galaxy inclination. Dashed lines connect the the Fe II (blue) and Mg II (red) measurements. For both tracers, lower inclination (more face-on) galaxies exhibit both larger EWs and more blueshifted velocities, compared to higher inclination (more edge-on) systems. The Low- and High-inclination bins differ by 2.3σ for Fe II and 3.2σ for Mg II. The observed inclination dependence suggests that outflows are collimated and preferentially launched perpendicular to the galactic plane.

and measured strength of the outflow varies with the viewing angle, consistent with a collimated geometry.

This picture is reproduced in simulations, in which outflows are preferentially launched perpendicular to the disk (Brook et al. 2011; Glasow et al. 2013; Fielding et al. 2017; Nelson et al. 2019). These simulations also show that outflowing gas is concentrated along the minor axis, while inflowing material is along the major axis (Péroux et al. 2020). In this model, feedback produces winds that escape along directions normal to the disk, leading to a bipolar structure.

Observations across a wide range of redshifts further support this interpretation. In the local universe ($z \sim 0.1$), this geometry is strongly suggested by Na D absorption measurements, where galaxies viewed more face-on exhibit larger blueshifts than more edge-on systems (Heckman et al. 2000; Chen et al. 2010; Roberts-Borsani & Saintonge 2019). Similar inclination trends have been reported in Mg II and Fe II absorption observations at $0.3 \lesssim z \lesssim 1.4$, which find decreasing outflow strength and detection fraction with increasing inclination (Bordoloi et al. 2011; Kornei et al. 2012; Kacprzak et al. 2012; Rubin et al. 2014; Guo et al. 2023). A comparable trend is also observed at higher redshift ($z \sim 2$), where outflow strength and detection fraction increase with decreasing inclination (Newman et al. 2012). How-

ever, this trend is not consistently recovered at $z \geq 2$, with many studies reporting no significant inclination dependence (Law et al. 2012; Förster Schreiber et al. 2019; Weldon et al. 2022), likely due to the more irregular morphologies of high-redshift galaxies, which make it more difficult to robustly measure inclinations.

In general, inclination trends are consistent with collimated outflows, where the observed outflow becomes stronger as the galaxy is viewed more face-on. The clear trend measured in our sample (Figure 14), where lower inclination (more face-on) galaxies exhibit larger EWs and more blueshifted outflow velocities, provides direct evidence for collimated outflows at earlier times.

5.3. Geometry of Inflowing Gas

Our result that inflows are preferentially detected in highly inclined galaxies (Figure 12) indicates that geometry influences the detectability of inflowing gas. This trend is evident across all three tracers, with 4 out of 5 (80%) of Fe II inflows, 11 out of 12 (92%) of Mg II inflows, and 2 out of 2 (100%) of Na D inflows detected in galaxies with inclinations greater than 50° . In support of this picture, the galaxy in our sample with the fastest inflow, SSA22-20013 (Figure 6), is also highly inclined (79°). The increased incidence of inflows in higher inclination (more edge-on) galaxies suggests that the gas producing the redshifted absorption is likely concentrated near the galactic plane rather than distributed isotropically throughout the system. With this geometry, inflow velocities are more easily detected when the galaxy is being viewed edge-on because gas moving within or close to the plane produces a larger line of sight velocity component. When the galaxy is closer to being viewed face-on (lower inclinations), these inflows project weakly along the line of sight, making them more difficult to detect even when they are present. This implies that part of the low detection rate of inflows may be driven by the orientation of the galaxy with respect to the observer rather than by an intrinsic lack of accretion as already suggested by lower-redshift studies.

This interpretation is supported by cosmological simulations, which show that inflow rates depend strongly on the azimuthal angle and are stronger along the major axis, where gas is funneled inward toward galaxies (Péroux et al. 2020). In these simulations, galaxies are supplied by narrow, dense streams of cold gas that deliver material along the major axis, often closely aligned with the disk plane (Fumagalli et al. 2011). Cosmological simulations further show that accreting cool gas carries substantial angular momentum and often forms extended, warped, co-rotating structures that flow around the galactic disk (Stewart et al. 2011). This geometry

produces stronger inflow velocities in edge-on systems, consistent with the inclination dependence observed in our sample.

Observations also support this geometry of inflowing gas. At $z \leq 1$, redshifted Fe II and Mg II absorption is more often detected in higher inclined galaxies. For example, Rubin et al. (2012) identified six galaxies with inflows and found that five out of the six were among the most edge-on galaxies in their sample. Similarly, Ho et al. (2017) examined Mg II absorption for galaxies at $0.15 < z < 0.3$ and found that the absorbing gas around highly inclined galaxies frequently shares the rotational direction of the galactic disk, suggesting that inflowing material may rotate with the galaxy before spiraling inward. A similar inclination dependence is observed with Na D for local galaxies ($z \sim 0.1$). In these galaxies, the line center shifts toward redder wavelengths as inclination increases, with inflows only being detected at $i \gtrsim 50^\circ$ (Chen et al. 2010; Roberts-Borsani & Saintonge 2019). These observations show that the inclination dependence observed in our sample is not unique, but instead reflects a broader trend across multiple tracers and redshift ranges.

Both simulations and observations indicate that the redshifted absorption detected in our sample traces inflowing gas that is distributed near the plane of the galactic disk. The consistency of this inclination dependence across multiple tracers and redshifts suggests that accretion along the disk may be a common characteristic of cool gas inflows onto galaxies.

5.4. Physical Drivers of Mg II Emission

We observe significant Mg II emission in 8% of our sample and find that Mg II emitters have lower M_* , lower (more negative) β , and higher sSFRs and H α and [O III] emission EWs compared to non-emitters (Figure 13; Hayes et al. 2025). Our results also show that the Mg II absorption EW decreases with decreasing M_* , SFR, and A_V (Figure 11). These trends indicate that Mg II emission is favored in low-mass, actively star-forming, dust-poor galaxies, whereas stronger absorption is associated with more massive and dustier galaxies. Our findings build directly on the results presented in our previous work (Kehoe et al. 2025), where we showed that Mg II emitters at $z \gtrsim 2$ preferentially exhibit lower M_* , bluer β , lower A_V and higher sSFRs compared to non-emitters. Our current results additionally show that Mg II emitters exhibit higher H α and [O III] emission EWs, linking Mg II emission to intense recent star formation. These trends are also consistent with other studies, which find that Mg II emitters are often found among galaxies with $M_* \lesssim 10^{10} M_\odot$, low A_V , and high

sSFR (e.g., Weiner et al. 2009; Rubin et al. 2010; Erb et al. 2012; Kornei et al. 2012; Guseva et al. 2013, 2019; Zhu et al. 2015; Finley et al. 2017; Feltre et al. 2018).

One of the strongest trends for Mg II emission is the dependence on both M_* and A_V . Observations at $1 \lesssim z \lesssim 2$ show that Mg II emission strength decreases in more massive and dustier galaxies (Kornei et al. 2012; Erb et al. 2012; Feltre et al. 2018). This behavior is generally attributed to the increase in ISM column density and dust content in more massive systems, which alters the escape of resonantly scattered photons. In this regime – as is the case for Ly α (e.g., Shapley et al. 2003) – Mg II photons undergo multiple scatterings, which increases their effective path length through the ISM, leading to a higher probability of dust absorption (Prochaska et al. 2011; Scarlata & Panagia 2015; Zhu et al. 2015; Feltre et al. 2018; Henry et al. 2018; Katz et al. 2022; Xu et al. 2023; Garel et al. 2024). Consequently, Mg II is strongly attenuated in high A_V objects, making Mg II emission more likely to be detected in low mass, dust-poor galaxies. This interpretation is also consistent with the observed β trend, where bluer slopes in Mg II emitters indicate lower A_V and more efficient escape of resonantly scattered photons.

The connection between Mg II emission and sSFR further supports this picture. In our sample, Mg II emitters exhibit elevated sSFRs, indicating that strong emission is generally associated with galaxies undergoing intense, recent star formation. Earlier work at $z \sim 1$ similarly finds that Mg II emission strength increases with sSFR (Kornei et al. 2012; Rubin et al. 2014). This suggests that Mg II emission arises from nebular photon production in actively star-forming regions, where lower A_V further enhances the escape of the emitted photons. We also find that the Mg II absorption EW decreases with decreasing SFR, consistent with previous work at $1 < z < 2$, showing that stronger Mg II emission was found in galaxies with lower SFRs (Weiner et al. 2009; Erb et al. 2012). Erb et al. (2012) further note that the SFR dependence is weaker than the trends found with M_* and A_V , suggesting that the observed SFR trend may be secondary and driven by underlying correlations with M_* and A_V .

The physical conditions inferred for the Mg II emitters also resemble those commonly associated with LyC-leaking galaxies (Jaskot & Oey 2013; Izotov et al. 2016; Finley et al. 2017; Henry et al. 2018; Chisholm et al. 2020; Katz et al. 2022; Flury et al. 2022a,b). These galaxies are typically low-mass, metal-poor galaxies with elevated specific star formation rates and extreme nebular emission properties. This similarity arises because Mg II and Ly α are governed by resonant scattering in

the neutral ISM and CGM, making them sensitive to the same underlying gas distribution. Ly α escape has been linked to the LyC escape fraction (f_{esc}) in both observations and theoretical studies (Verhamme et al. 2017; Gazagnes et al. 2020; Izotov et al. 2021; Pahl et al. 2021; Flury et al. 2022b; Choustikov et al. 2024; Le Reste et al. 2025). However, at high redshift ($z \geq 6$), corresponding to the epoch of reionization, Ly α becomes increasingly attenuated by the neutral IGM, making it difficult to use as a tracer of f_{esc} .

Mg II can be used as an alternative probe, as an indirect indicator of f_{esc} , because its ionization potential is close to that of neutral hydrogen and it traces the neutral gas conditions that regulate f_{esc} (Henry et al. 2018; Chisholm et al. 2020; Chang & Gronke 2024). Observational studies at low redshift ($z < 0.5$) have demonstrated that Mg II can be used as an indirect tracer of the LyC escape fraction (Chisholm et al. 2020; Izotov et al. 2022; Xu et al. 2022, 2023; Leclercq et al. 2024). Recently, this has been extended to the epoch of reionization, where Mg II was used to place constraints on f_{esc} at $z \sim 7.5$ (Gazagnes et al. 2025). Comparisons with simulations (Katz et al. 2022) suggested that these Mg II-based estimates overpredict f_{esc} and should only be used as upper limits, implying only weak LyC leakage for these high redshift galaxies (Gazagnes et al. 2025). Our results, showing a clear preference for Mg II emission in low-mass, dust-poor, high sSFR galaxies with strong nebular emission, supports the use of Mg II as an indirect tracer of f_{esc} , providing an alternative and more robust tracer for high redshift galaxies in the epoch of reionization.

6. CONCLUSIONS

We have presented a joint analysis of NUV Fe II and Mg II and optical Na D absorption kinematics using a combined *JWST*/NIRSpec sample drawn from the LyC22, EXCELS, and AURORA surveys at $z_{\text{med}} = 3.07$. This work builds on the results of Kehoe et al. (2025), which was based solely on the AURORA survey, by significantly expanding the sample size through the inclusion of additional NIRSpec programs. By combining these datasets, we have constructed a large and diverse sample of 321 star-forming galaxies with measurements of low-ionization absorption tracers, enabling a detailed study of outflow and inflow properties across a wide range of galaxy masses, star formation rates, and dust content. Our analysis focuses on how gas kinematics traced by Fe II, Mg II, and Na D absorption depends on galaxy properties and viewing geometry. Our main results are as follows:

1. We find no statistically significant correlation between individual or composite NUV outflow velocity measurements and any galaxy property. However, galaxies with detected NUV outflows are preferentially located at higher M_* , SFR, and Σ_{SFR} , suggesting that more massive and stronger star-forming galaxies are more likely to host detectable outflows.
2. The absorption EWs of Fe II and Mg II absorption increases with M_* , SFR, nebular $E(B - V)$, and stellar A_V , indicating that variations in NUV absorption strength are primarily driven by changes in column density and covering fraction of low-ionization gas rather than changes in outflow velocity.
3. Na D absorption shows no correlation between outflow velocity and any galaxy properties, but does exhibit higher absorption EWs and a higher incidence of outflow detections in more massive, dusty, and actively star-forming galaxies.
4. The composite spectra reveal a strong dependence between outflow kinematics and galaxy inclination, with more face-on systems exhibiting larger absorption EWs and higher maximum outflow velocities in the NUV absorption lines. This result provides direct observational evidence that star-formation driven outflows at $z \sim 3$ are collimated, and are preferentially directed along the minor axis.
5. The inflowing gas traced by redshifted absorption is more biased toward highly inclined (more edge-on) galaxies, suggesting that accretion primarily occurs in or near the galactic disk plane, rather than isotropically distributed throughout the halo.
6. Mg II emission is predominantly observed in galaxies with low M_* , low dust content, and high sSFR, consistent with efficient escape of resonantly scattered photons in objects with lower neutral gas content and dust attenuation. These conditions are similar to those associated with elevated ionizing f_{esc} , suggesting that Mg II may trace conditions favorable for ionizing photon escape. Mg II emitters also exhibit higher H α and [O III] emission EWs, indicating that Mg II emission may be linked to young, high sSFR objects with hard ionizing conditions.

Our results demonstrate that while scaling relations between outflow velocity and galaxy properties are weak or absent in our sample, both the detectability and

strength of both inflows and outflows are strongly governed by galaxy orientation. We find the first observational evidence at $z \sim 3$ for a structured, directionally dependent gas flow geometry, with bipolar outflows emerging perpendicular to the disk and inflowing gas co-rotating along the galactic plane. This geometric interpretation explains the dependence of absorption strength and detection rates on viewing angle and highlights the importance of orientation in shaping low-ionization gas kinematics. We find that these trends are consistent with simulations (e.g. Fumagalli et al. 2011; Nelson et al. 2019; Péroux et al. 2020) and low-redshift ($z \lesssim 1$) studies (e.g. Chen et al. 2010; Kacprzak et al. 2012; Ho et al. 2017), which find that outflows are bipolar and perpendicular to the galactic disk, while inflows are co-rotating along the major axis.

The lack of strong correlations between outflow velocity and galaxy properties likely reflects the limited dynamic range of our sample in M_* and SFR, as well as the large fraction of low S/N spectra, which may hide weaker absorption features. Future *JWST* surveys with larger and more diverse samples, particularly extending to lower-mass and lower-SFR regimes and improved S/N for individual spectra will be essential to search for correlations more robustly. Extending such analyses to higher redshift, where both rest-frame FUV and NUV tracers can be covered within the same spectra (Kehoe et al. 2025), will also enable more direct comparisons of gas flow kinematics across multiple transitions of the same gas phase.

This work is based on observations made with the NASA/ESA/CSA James Webb Space Telescope. The data were obtained from the Mikulski Archive for Space Telescopes at the Space Telescope Science Institute, which is operated by the Association of Universities for Research in Astronomy, Inc., under NASA contract NAS5-03127 for JWST. The specific observations analyzed can be accessed via DOI: [10.17909/6mza-5q55](https://doi.org/10.17909/6mza-5q55), DOI: [10.17909/4r31-j678](https://doi.org/10.17909/4r31-j678), and DOI: [10.17909/sqde-1112](https://doi.org/10.17909/sqde-1112). We also acknowledge support from NASA grants JWST-GO-01914, GO-01869, and GO-03543. ACC, LT, and HL acknowledge support from a UKRI Frontier Research Grantee Grant (PI Carnall; grant reference EP/Y037065/1). DJM acknowledge the support of the Royal Society through the award of a Royal Society University Research Professorship to Prof. James Dunlop. AKI acknowledge support from JSPS KAKENHI 26H02069, 25K00020, 24H00002, and 23H00131. YI and NGG acknowledge support from the National Academy of Sciences of Ukraine by its project no. 0126U000353. SDS acknowledges support from a UKRI Frontier Research Guarantee Grant (PI Carnall; grant reference EP/Y037065/1). ASL acknowledges support from Knut and Alice Wallenberg Foundation. MS acknowledges support for Program number JWST-GO-03543.014 that was provided through a grant from the STScI under NASA contract NAS5-03127.

REFERENCES

- Avery, C. R., Wuyts, S., Förster Schreiber, N. M., et al. 2022, *Monthly Notices of the Royal Astronomical Society*, 511, 4223, doi: [10.1093/mnras/stac190](https://doi.org/10.1093/mnras/stac190)
- Bauermeister, A., Blitz, L., & Ma, C.-P. 2010, *The Astrophysical Journal*, 717, 323, doi: [10.1088/0004-637X/717/1/323](https://doi.org/10.1088/0004-637X/717/1/323)
- Belli, S., Park, M., Davies, R. L., et al. 2024, *Nature*, 630, 54, doi: [10.1038/s41586-024-07412-1](https://doi.org/10.1038/s41586-024-07412-1)
- Bertin, E., Schefer, M., Apostolakis, N., et al. 2020, in *Astronomical Society of the Pacific Conference Series*, Vol. 527, *Astronomical Data Analysis Software and Systems XXIX*, ed. R. Pizzo, E. R. Deul, J. D. Mol, J. de Plaa, & H. Verkouter, 461
- Bevacqua, D., Marchesini, D., Saracco, P., et al. 2026, *The Astrophysical Journal*, 997, 189, doi: [10.3847/1538-4357/ae247c](https://doi.org/10.3847/1538-4357/ae247c)
- Birrer, S. 2021, *ApJ*, 919, 38, doi: [10.3847/1538-4357/ac1108](https://doi.org/10.3847/1538-4357/ac1108)
- Birrer, S., Bhamre, V., Nierenberg, A., Yang, L., & Van de Vyvere, L. 2022, PSFr: Point Spread Function reconstruction, *Astrophysics Source Code Library*, record ascl:2210.005. <http://ascl.net/2210.005>
- Bordoloi, R., Lilly, S. J., Knobel, C., et al. 2011, *ApJ*, 743, 10, doi: [10.1088/0004-637X/743/1/10](https://doi.org/10.1088/0004-637X/743/1/10)
- Bordoloi, R., Lilly, S. J., Hardmeier, E., et al. 2014, *ApJ*, 794, 130, doi: [10.1088/0004-637X/794/2/130](https://doi.org/10.1088/0004-637X/794/2/130)
- Bradshaw, E. J., Almaini, O., Hartley, W. G., et al. 2013, *MNRAS*, 433, 194, doi: [10.1093/mnras/stt715](https://doi.org/10.1093/mnras/stt715)
- Brook, C. B., Governato, F., Roškar, R., et al. 2011, *Monthly Notices of the Royal Astronomical Society*, 415, 1051, doi: [10.1111/j.1365-2966.2011.18545.x](https://doi.org/10.1111/j.1365-2966.2011.18545.x)
- Calabrò, A., Pentericci, L., Talia, M., et al. 2022, *A&A*, 667, A117, doi: [10.1051/0004-6361/202244364](https://doi.org/10.1051/0004-6361/202244364)
- Calzetti, D., Armus, L., Bohlin, R. C., et al. 2000, *ApJ*, 533, 682, doi: [10.1086/308692](https://doi.org/10.1086/308692)
- Cardelli, J. A., Clayton, G. C., & Mathis, J. S. 1989, *ApJ*, 345, 245, doi: [10.1086/167900](https://doi.org/10.1086/167900)

- Carnall, A. C., Leja, J., Johnson, B. D., et al. 2019, *The Astrophysical Journal*, 873, 44, doi: [10.3847/1538-4357/ab04a2](https://doi.org/10.3847/1538-4357/ab04a2)
- Carnall, A. C., McLure, R. J., Dunlop, J. S., & Davé, R. 2018, *Monthly Notices of the Royal Astronomical Society*, 480, 4379, doi: [10.1093/mnras/sty2169](https://doi.org/10.1093/mnras/sty2169)
- Carnall, A. C., Cullen, F., McLure, R. J., et al. 2024, *MNRAS*, 534, 325, doi: [10.1093/mnras/stae2092](https://doi.org/10.1093/mnras/stae2092)
- Carniani, S., Venturi, G., Parlanti, E., et al. 2024, *A&A*, 685, A99, doi: [10.1051/0004-6361/202347230](https://doi.org/10.1051/0004-6361/202347230)
- Chabrier, G. 2003, *PASP*, 115, 763, doi: [10.1086/376392](https://doi.org/10.1086/376392)
- Chang, S.-J., & Gronke, M. 2024, *Monthly Notices of the Royal Astronomical Society*, 532, 3526, doi: [10.1093/mnras/stae1664](https://doi.org/10.1093/mnras/stae1664)
- Chen, Y.-M., Tremonti, C. A., Heckman, T. M., et al. 2010, *AJ*, 140, 445, doi: [10.1088/0004-6256/140/2/445](https://doi.org/10.1088/0004-6256/140/2/445)
- Chisholm, J., Prochaska, J. X., Schaerer, D., Gazagnes, S., & Henry, A. 2020, *MNRAS*, 498, 2554, doi: [10.1093/mnras/staa2470](https://doi.org/10.1093/mnras/staa2470)
- Chisholm, J., Tremonti, C. A., Leitherer, C., & Chen, Y. 2017, *Monthly Notices of the Royal Astronomical Society*, 469, 4831, doi: [10.1093/mnras/stx1164](https://doi.org/10.1093/mnras/stx1164)
- Choustikov, N., Katz, H., Saxena, A., et al. 2024, *Monthly Notices of the Royal Astronomical Society*, 532, 2463, doi: [10.1093/mnras/stae1586](https://doi.org/10.1093/mnras/stae1586)
- Clarke, L., Shapley, A. E., Sanders, R. L., et al. 2024, *ApJ*, 977, 133, doi: [10.3847/1538-4357/ad8ba4](https://doi.org/10.3847/1538-4357/ad8ba4)
- Conroy, C., Gunn, J. E., & White, M. 2009, *ApJ*, 699, 486, doi: [10.1088/0004-637X/699/1/486](https://doi.org/10.1088/0004-637X/699/1/486)
- Davies, R. L., Belli, S., Park, M., et al. 2024, *MNRAS*, 528, 4976, doi: [10.1093/mnras/stae327](https://doi.org/10.1093/mnras/stae327)
- D'Eugenio, F., Pérez-González, P. G., Maiolino, R., et al. 2024, *Nature Astronomy*, 8, 1443, doi: [10.1038/s41550-024-02345-1](https://doi.org/10.1038/s41550-024-02345-1)
- Di Matteo, T., Springel, V., & Hernquist, L. 2005, *Nature*, 433, 604, doi: [10.1038/nature03335](https://doi.org/10.1038/nature03335)
- Du, X., Shapley, A. E., Topping, M. W., et al. 2021, *ApJ*, 920, 95, doi: [10.3847/1538-4357/ac1273](https://doi.org/10.3847/1538-4357/ac1273)
- Eisenstein, D. J., Willott, C., Alberts, S., et al. 2026, *ApJS*, 283, 6, doi: [10.3847/1538-4365/ae3163](https://doi.org/10.3847/1538-4365/ae3163)
- Eldridge, J. J., Stanway, E. R., Xiao, L., et al. 2017, *Publications of the Astronomical Society of Australia*, 34, e058, doi: [10.1017/pasa.2017.51](https://doi.org/10.1017/pasa.2017.51)
- Erb, D. K. 2015, *Nature*, 523, 169, doi: [10.1038/nature14454](https://doi.org/10.1038/nature14454)
- Erb, D. K., Quider, A. M., Henry, A. L., & Martin, C. L. 2012, *The Astrophysical Journal*, 759, 26, doi: [10.1088/0004-637X/759/1/26](https://doi.org/10.1088/0004-637X/759/1/26)
- Faucher-Giguère, C.-A., & Kereš, D. 2011, *Monthly Notices of the Royal Astronomical Society: Letters*, 412, L118, doi: [10.1111/j.1745-3933.2011.01018.x](https://doi.org/10.1111/j.1745-3933.2011.01018.x)
- Feltre, A., Bacon, R., Tresse, L., et al. 2018, *A&A*, 617, A62, doi: [10.1051/0004-6361/201833281](https://doi.org/10.1051/0004-6361/201833281)
- Fielding, D., Quataert, E., Martizzi, D., & Faucher-Giguère, C.-A. 2017, *Monthly Notices of the Royal Astronomical Society: Letters*, 470, L39, doi: [10.1093/mnrasl/slx072](https://doi.org/10.1093/mnrasl/slx072)
- Finley, H., Bouché, N., Contini, T., et al. 2017, *A&A*, 608, A7, doi: [10.1051/0004-6361/201731499](https://doi.org/10.1051/0004-6361/201731499)
- Flury, S. R., Jaskot, A. E., Ferguson, H. C., et al. 2022a, *ApJS*, 260, 1, doi: [10.3847/1538-4365/ac5331](https://doi.org/10.3847/1538-4365/ac5331)
- . 2022b, *ApJ*, 930, 126, doi: [10.3847/1538-4357/ac61e4](https://doi.org/10.3847/1538-4357/ac61e4)
- Foreman-Mackey, D., Hogg, D. W., Lang, D., & Goodman, J. 2013, *PASP*, 125, 306, doi: [10.1086/670067](https://doi.org/10.1086/670067)
- Fumagalli, M., Prochaska, J. X., Kasen, D., et al. 2011, *MNRAS*, 418, 1796, doi: [10.1111/j.1365-2966.2011.19599.x](https://doi.org/10.1111/j.1365-2966.2011.19599.x)
- Förster Schreiber, N. M., Übler, H., Davies, R. L., et al. 2019, *The Astrophysical Journal*, 875, 21, doi: [10.3847/1538-4357/ab0ca2](https://doi.org/10.3847/1538-4357/ab0ca2)
- Garel, T., Michel-Dansac, L., Verhamme, A., et al. 2024, *A&A*, 691, A213, doi: [10.1051/0004-6361/202450654](https://doi.org/10.1051/0004-6361/202450654)
- Gazagnes, S., Chisholm, J., Schaerer, D., Verhamme, A., & Izotov, Y. 2020, *A&A*, 639, A85, doi: [10.1051/0004-6361/202038096](https://doi.org/10.1051/0004-6361/202038096)
- Gazagnes, S., Chisholm, J., Endsley, R., et al. 2025, *Monthly Notices of the Royal Astronomical Society*, 540, 2331, doi: [10.1093/mnras/staf768](https://doi.org/10.1093/mnras/staf768)
- Genin, A., Shuntov, M., Brammer, G., et al. 2025, *A&A*, 699, A343, doi: [10.1051/0004-6361/202555504](https://doi.org/10.1051/0004-6361/202555504)
- Giavalisco, M., Vanzella, E., Salimbeni, S., et al. 2011, *The Astrophysical Journal*, 743, 95, doi: [10.1088/0004-637X/743/1/95](https://doi.org/10.1088/0004-637X/743/1/95)
- Glasow, W. v., Krause, M. G. H., Sommer-Larsen, J., & Burkert, A. 2013, *Monthly Notices of the Royal Astronomical Society*, 434, 1151, doi: [10.1093/mnras/stt1060](https://doi.org/10.1093/mnras/stt1060)
- Gordon, K. D., Clayton, G. C., Misselt, K. A., Landolt, A. U., & Wolff, M. J. 2003, *The Astrophysical Journal*, 594, 279, doi: [10.1086/376774](https://doi.org/10.1086/376774)
- Guo, Y., Bacon, R., Bouché, N. F., et al. 2023, *Nature*, 624, 53, doi: [10.1038/s41586-023-06718-w](https://doi.org/10.1038/s41586-023-06718-w)
- Guseva, N. G., Izotov, Y. I., Fricke, K. J., & Henkel, C. 2013, *A&A*, 555, A90, doi: [10.1051/0004-6361/201221010](https://doi.org/10.1051/0004-6361/201221010)
- . 2019, *A&A*, 624, A21, doi: [10.1051/0004-6361/201834935](https://doi.org/10.1051/0004-6361/201834935)
- Hayes, M. J., Saldana-Lopez, A., Citro, A., et al. 2025, *ApJ*, 982, 14, doi: [10.3847/1538-4357/adaea1](https://doi.org/10.3847/1538-4357/adaea1)

- Heckman, T. M., Alexandroff, R. M., Borthakur, S., Overzier, R., & Leitherer, C. 2015, *ApJ*, 809, 147, doi: [10.1088/0004-637X/809/2/147](https://doi.org/10.1088/0004-637X/809/2/147)
- Heckman, T. M., Armus, L., & Miley, G. K. 1990, *ApJS*, 74, 833, doi: [10.1086/191522](https://doi.org/10.1086/191522)
- Heckman, T. M., & Borthakur, S. 2016, *ApJ*, 822, 9, doi: [10.3847/0004-637X/822/1/9](https://doi.org/10.3847/0004-637X/822/1/9)
- Heckman, T. M., Lehnert, M. D., Strickland, D. K., & Armus, L. 2000, *The Astrophysical Journal Supplement Series*, 129, 493, doi: [10.1086/313421](https://doi.org/10.1086/313421)
- Henry, A., Berg, D. A., Scarlata, C., Verhamme, A., & Erb, D. 2018, *ApJ*, 855, 96, doi: [10.3847/1538-4357/aab099](https://doi.org/10.3847/1538-4357/aab099)
- Ho, S. H., Martin, C. L., Kacprzak, G. G., & Churchill, C. W. 2017, *The Astrophysical Journal*, 835, 267, doi: [10.3847/1538-4357/835/2/267](https://doi.org/10.3847/1538-4357/835/2/267)
- Hopkins, P. F., Cox, T. J., Kereš, D., & Hernquist, L. 2008, *The Astrophysical Journal Supplement Series*, 175, 390, doi: [10.1086/524363](https://doi.org/10.1086/524363)
- Izotov, Y. I., Chisholm, J., Worseck, G., et al. 2022, *MNRAS*, 515, 2864, doi: [10.1093/mnras/stac1899](https://doi.org/10.1093/mnras/stac1899)
- Izotov, Y. I., Schaerer, D., Thuan, T. X., et al. 2016, *MNRAS*, 461, 3683, doi: [10.1093/mnras/stw1205](https://doi.org/10.1093/mnras/stw1205)
- Izotov, Y. I., Worseck, G., Schaerer, D., et al. 2021, *Monthly Notices of the Royal Astronomical Society*, 503, 1734, doi: [10.1093/mnras/stab612](https://doi.org/10.1093/mnras/stab612)
- Jaskot, A. E., & Oey, M. S. 2013, *ApJ*, 766, 91, doi: [10.1088/0004-637X/766/2/91](https://doi.org/10.1088/0004-637X/766/2/91)
- Kacprzak, G. G. 2017, in *Astrophysics and Space Science Library*, Vol. 430, *Gas Accretion onto Galaxies*, ed. A. Fox & R. Davé, 145, doi: [10.1007/978-3-319-52512-9_7](https://doi.org/10.1007/978-3-319-52512-9_7)
- Kacprzak, G. G., Churchill, C. W., & Nielsen, N. M. 2012, *ApJL*, 760, L7, doi: [10.1088/2041-8205/760/1/L7](https://doi.org/10.1088/2041-8205/760/1/L7)
- Katz, H., Garel, T., Rosdahl, J., et al. 2022, *Monthly Notices of the Royal Astronomical Society*, 515, 4265, doi: [10.1093/mnras/stac1437](https://doi.org/10.1093/mnras/stac1437)
- Kehoe, E., Shapley, A. E., Schreiber, N. M. F., et al. 2024, *ApJ*, 976, 28, doi: [10.3847/1538-4357/ad7ebb](https://doi.org/10.3847/1538-4357/ad7ebb)
- Kehoe, E., Shapley, A. E., Sanders, R. L., et al. 2025, *The Astrophysical Journal*, 994, 170, doi: [10.3847/1538-4357/ae10b3](https://doi.org/10.3847/1538-4357/ae10b3)
- Kennicutt, Jr., R. C. 1989, *ApJ*, 344, 685, doi: [10.1086/167834](https://doi.org/10.1086/167834)
- Kimm, T., Slyz, A., Devriendt, J., & Pichon, C. 2011, *MNRAS*, 413, L51, doi: [10.1111/j.1745-3933.2011.01031.x](https://doi.org/10.1111/j.1745-3933.2011.01031.x)
- Kornei, K. A., Shapley, A. E., Martin, C. L., et al. 2012, *ApJ*, 758, 135, doi: [10.1088/0004-637X/758/2/135](https://doi.org/10.1088/0004-637X/758/2/135)
- . 2013, *ApJ*, 774, 50, doi: [10.1088/0004-637X/774/1/50](https://doi.org/10.1088/0004-637X/774/1/50)
- Kriek, M., van Dokkum, P. G., Labbé, I., et al. 2009, *The Astrophysical Journal*, 700, 221, doi: [10.1088/0004-637X/700/1/221](https://doi.org/10.1088/0004-637X/700/1/221)
- Kroupa, P. 2001, *Monthly Notices of the Royal Astronomical Society*, 322, 231, doi: [10.1046/j.1365-8711.2001.04022.x](https://doi.org/10.1046/j.1365-8711.2001.04022.x)
- Law, D. R., Steidel, C. C., Shapley, A. E., et al. 2012, *The Astrophysical Journal*, 759, 29, doi: [10.1088/0004-637X/759/1/29](https://doi.org/10.1088/0004-637X/759/1/29)
- Le Reste, A., Scarlata, C., Hayes, M. J., et al. 2025, *ApJS*, 280, 27, doi: [10.3847/1538-4365/adf227](https://doi.org/10.3847/1538-4365/adf227)
- Leclercq, F., Chisholm, J., King, W., et al. 2024, *A&A*, 687, A73, doi: [10.1051/0004-6361/202449362](https://doi.org/10.1051/0004-6361/202449362)
- Leitherer, C., Tremonti, C. A., Heckman, T. M., & Calzetti, D. 2011, *The Astronomical Journal*, 141, 37, doi: [10.1088/0004-6256/141/2/37](https://doi.org/10.1088/0004-6256/141/2/37)
- Leroy, A. K., Walter, F., Brinks, E., et al. 2008, *The Astronomical Journal*, 136, 2782, doi: [10.1088/0004-6256/136/6/2782](https://doi.org/10.1088/0004-6256/136/6/2782)
- Lyu, C., Yu, H., Wang, E., et al. 2026, *ApJL*, 1000, L3, doi: [10.3847/2041-8213/ae48ee](https://doi.org/10.3847/2041-8213/ae48ee)
- Martin, C. L. 2005, *ApJ*, 621, 227, doi: [10.1086/427277](https://doi.org/10.1086/427277)
- Martin, C. L., Shapley, A. E., Coil, A. L., et al. 2012, *ApJ*, 760, 127, doi: [10.1088/0004-637X/760/2/127](https://doi.org/10.1088/0004-637X/760/2/127)
- . 2013, *ApJ*, 770, 41, doi: [10.1088/0004-637X/770/1/41](https://doi.org/10.1088/0004-637X/770/1/41)
- Moretti, L., Belli, S., Rudie, G. C., et al. 2026, *A&A*, 707, A146, doi: [10.1051/0004-6361/202556336](https://doi.org/10.1051/0004-6361/202556336)
- Murray, N., Ménard, B., & Thompson, T. A. 2011, *The Astrophysical Journal*, 735, 66, doi: [10.1088/0004-637X/735/1/66](https://doi.org/10.1088/0004-637X/735/1/66)
- Nelson, D., Pillepich, A., Springel, V., et al. 2019, *MNRAS*, 490, 3234, doi: [10.1093/mnras/stz2306](https://doi.org/10.1093/mnras/stz2306)
- Newman, S. F., Genzel, R., Förster-Schreiber, N. M., et al. 2012, *The Astrophysical Journal*, 761, 43, doi: [10.1088/0004-637X/761/1/43](https://doi.org/10.1088/0004-637X/761/1/43)
- Pahl, A. J., Shapley, A., Steidel, C. C., Chen, Y., & Reddy, N. A. 2021, *Monthly Notices of the Royal Astronomical Society*, 505, 2447, doi: [10.1093/mnras/stab1374](https://doi.org/10.1093/mnras/stab1374)
- Pahl, A. J., Shapley, A., Steidel, C. C., Reddy, N. A., & Chen, Y. 2022, *Monthly Notices of the Royal Astronomical Society*, 516, 2062, doi: [10.1093/mnras/stac1767](https://doi.org/10.1093/mnras/stac1767)
- Pasha, I., & Miller, T. B. 2023, *The Journal of Open Source Software*, 8, 5703, doi: [10.21105/joss.05703](https://doi.org/10.21105/joss.05703)
- Prochaska, J. X., Kasen, D., & Rubin, K. 2011, *The Astrophysical Journal*, 734, 24, doi: [10.1088/0004-637X/734/1/24](https://doi.org/10.1088/0004-637X/734/1/24)
- Prochaska, J. X., & Wolfe, A. M. 2009, *The Astrophysical Journal*, 696, 1543, doi: [10.1088/0004-637X/696/2/1543](https://doi.org/10.1088/0004-637X/696/2/1543)
- Prusinski, N. Z., Erb, D. K., & Martin, C. L. 2021, *AJ*, 161, 212, doi: [10.3847/1538-3881/abe85b](https://doi.org/10.3847/1538-3881/abe85b)

- Péroux, C., Nelson, D., van de Voort, F., et al. 2020, *Monthly Notices of the Royal Astronomical Society*, 499, 2462, doi: [10.1093/mnras/staa2888](https://doi.org/10.1093/mnras/staa2888)
- Reddy, N. A., Topping, M. W., Shapley, A. E., et al. 2022, *ApJ*, 926, 31, doi: [10.3847/1538-4357/ac3b4c](https://doi.org/10.3847/1538-4357/ac3b4c)
- Roberts-Borsani, G. W., & Saintonge, A. 2019, *MNRAS*, 482, 4111, doi: [10.1093/mnras/sty2824](https://doi.org/10.1093/mnras/sty2824)
- Rubin, K. H. R., Prochaska, J. X., Koo, D. C., et al. 2014, *The Astrophysical Journal*, 794, 156, doi: [10.1088/0004-637X/794/2/156](https://doi.org/10.1088/0004-637X/794/2/156)
- Rubin, K. H. R., Prochaska, J. X., Koo, D. C., et al. 2014, *ApJ*, 794, 156, doi: [10.1088/0004-637X/794/2/156](https://doi.org/10.1088/0004-637X/794/2/156)
- Rubin, K. H. R., Weiner, B. J., Koo, D. C., et al. 2010, *The Astrophysical Journal*, 719, 1503, doi: [10.1088/0004-637X/719/2/1503](https://doi.org/10.1088/0004-637X/719/2/1503)
- Rubin, K. H. R., Xavier Prochaska, J., Koo, D. C., & Phillips, A. C. 2012, *The Astrophysical Journal Letters*, 747, L26, doi: [10.1088/2041-8205/747/2/L26](https://doi.org/10.1088/2041-8205/747/2/L26)
- Rupke, D. S., Veilleux, S., & Sanders, D. B. 2005, *The Astrophysical Journal Supplement Series*, 160, 87, doi: [10.1086/432886](https://doi.org/10.1086/432886)
- Saintonge, A., Catinella, B., Tacconi, L. J., et al. 2017, *The Astrophysical Journal Supplement Series*, 233, 22, doi: [10.3847/1538-4365/aa97e0](https://doi.org/10.3847/1538-4365/aa97e0)
- Saldana-Lopez, A., Chisholm, J., Gazagnes, S., et al. 2025, *MNRAS*, 544, 132, doi: [10.1093/mnras/staf1680](https://doi.org/10.1093/mnras/staf1680)
- Salim, S., Boquien, M., & Lee, J. C. 2018, *The Astrophysical Journal*, 859, 11, doi: [10.3847/1538-4357/aabf3c](https://doi.org/10.3847/1538-4357/aabf3c)
- Sanders, R. L., Shapley, A. E., Topping, M. W., et al. 2025, *The Astrophysical Journal*, 989, 209, doi: [10.3847/1538-4357/adf066](https://doi.org/10.3847/1538-4357/adf066)
- Sanders, R. L., Shapley, A. E., Topping, M. W., et al. 2026, *ApJ*, 1003, 228, doi: [10.3847/1538-4357/ae66e2](https://doi.org/10.3847/1538-4357/ae66e2)
- Scannapieco, E., Silk, J., & Bouwens, R. 2005, *ApJL*, 635, L13, doi: [10.1086/499271](https://doi.org/10.1086/499271)
- Scarlata, C., & Panagia, N. 2015, *The Astrophysical Journal*, 801, 43, doi: [10.1088/0004-637X/801/1/43](https://doi.org/10.1088/0004-637X/801/1/43)
- Schaerer, D., Izotov, Y. I., Marques-Chaves, R., et al. 2026, *A&A*, 708, A242, doi: [10.1051/0004-6361/202556832](https://doi.org/10.1051/0004-6361/202556832)
- Shapley, A. E., Steidel, C. C., Pettini, M., & Adelberger, K. L. 2003, *ApJ*, 588, 65, doi: [10.1086/373922](https://doi.org/10.1086/373922)
- Shapley, A. E., Sanders, R. L., Topping, M. W., et al. 2025, *The Astrophysical Journal*, 980, 242, doi: [10.3847/1538-4357/adad68](https://doi.org/10.3847/1538-4357/adad68)
- Silk, J., & Rees, M. J. 1998, *A&A*, 331, L1, doi: [10.48550/arXiv.astro-ph/9801013](https://doi.org/10.48550/arXiv.astro-ph/9801013)
- Somerville, R. S., Hopkins, P. F., Cox, T. J., Robertson, B. E., & Hernquist, L. 2008, *MNRAS*, 391, 481, doi: [10.1111/j.1365-2966.2008.13805.x](https://doi.org/10.1111/j.1365-2966.2008.13805.x)
- Stanton, T. M., Cullen, F., Carnall, A. C., et al. 2026, *Monthly Notices of the Royal Astronomical Society*, stag449, doi: [10.1093/mnras/stag449](https://doi.org/10.1093/mnras/stag449)
- Stanway, E. R., & Eldridge, J. J. 2018, *Monthly Notices of the Royal Astronomical Society*, 479, 75, doi: [10.1093/mnras/sty1353](https://doi.org/10.1093/mnras/sty1353)
- Steidel, C. C., Bogosavljević, M., Shapley, A. E., et al. 2018, *The Astrophysical Journal*, 869, 123, doi: [10.3847/1538-4357/aaed28](https://doi.org/10.3847/1538-4357/aaed28)
- Steidel, C. C., Erb, D. K., Shapley, A. E., et al. 2010, *ApJ*, 717, 289, doi: [10.1088/0004-637X/717/1/289](https://doi.org/10.1088/0004-637X/717/1/289)
- Stewart, K. R., Kaufmann, T., Bullock, J. S., et al. 2011, *The Astrophysical Journal*, 738, 39, doi: [10.1088/0004-637X/738/1/39](https://doi.org/10.1088/0004-637X/738/1/39)
- Strickland, D. K., & Heckman, T. M. 2009, *ApJ*, 697, 2030, doi: [10.1088/0004-637X/697/2/2030](https://doi.org/10.1088/0004-637X/697/2/2030)
- Sun, Y., Ji, Z., Rieke, G. H., et al. 2025, arXiv e-prints, arXiv:2504.14682, doi: [10.48550/arXiv.2504.14682](https://doi.org/10.48550/arXiv.2504.14682)
- Tacconi, L. J., Genzel, R., Saintonge, A., et al. 2018, *The Astrophysical Journal*, 853, 179, doi: [10.3847/1538-4357/aaa4b4](https://doi.org/10.3847/1538-4357/aaa4b4)
- Talia, M., Mignoli, M., Cimatti, A., et al. 2012, *A&A*, 539, A61, doi: [10.1051/0004-6361/201117683](https://doi.org/10.1051/0004-6361/201117683)
- Taylor, E., Carnall, A. C., Maltby, D., et al. 2026, arXiv e-prints, arXiv:2601.02269, doi: [10.48550/arXiv.2601.02269](https://doi.org/10.48550/arXiv.2601.02269)
- Tombesi, F., Cappi, M., Reeves, J. N., et al. 2010, *A&A*, 521, A57, doi: [10.1051/0004-6361/200913440](https://doi.org/10.1051/0004-6361/200913440)
- Topping, M. W., Sanders, R. L., Shapley, A. E., et al. 2025, *Monthly Notices of the Royal Astronomical Society*, 541, 1707, doi: [10.1093/mnras/staf903](https://doi.org/10.1093/mnras/staf903)
- Tumlinson, J., Peebles, M. S., & Werk, J. K. 2017, *ARA&A*, 55, 389, doi: [10.1146/annurev-astro-091916-055240](https://doi.org/10.1146/annurev-astro-091916-055240)
- Tumlinson, J., Thom, C., Werk, J. K., et al. 2011, *Science*, 334, 948, doi: [10.1126/science.1209840](https://doi.org/10.1126/science.1209840)
- Valentino, F., Brammer, G., Gould, K. M. L., et al. 2023, *The Astrophysical Journal*, 947, 20, doi: [10.3847/1538-4357/acbefa](https://doi.org/10.3847/1538-4357/acbefa)
- Veilleux, S., Cecil, G., & Bland-Hawthorn, J. 2005, *Annual Review of Astronomy and Astrophysics*, 43, 769, doi: [https://doi.org/10.1146/annurev.astro.43.072103.150610](https://doi.org/https://doi.org/10.1146/annurev.astro.43.072103.150610)
- Verhamme, A., Orlitová, I., Schaerer, D., et al. 2017, *A&A*, 597, A13, doi: [10.1051/0004-6361/201629264](https://doi.org/10.1051/0004-6361/201629264)
- Weiner, B. J., Coil, A. L., Prochaska, J. X., et al. 2009, *The Astrophysical Journal*, 692, 187, doi: [10.1088/0004-637X/692/1/187](https://doi.org/10.1088/0004-637X/692/1/187)
- Weldon, A., Reddy, N. A., Topping, M. W., et al. 2022, *MNRAS*, 515, 841, doi: [10.1093/mnras/stac1822](https://doi.org/10.1093/mnras/stac1822)

- Weldon, A., Reddy, N. A., Topping, M. W., et al. 2023, Monthly Notices of the Royal Astronomical Society, 523, 5624, doi: [10.1093/mnras/stad1615](https://doi.org/10.1093/mnras/stad1615)
- Wisnioski, E., Förster Schreiber, N. M., Wuyts, S., et al. 2015, ApJ, 799, 209, doi: [10.1088/0004-637X/799/2/209](https://doi.org/10.1088/0004-637X/799/2/209)
- Wisnioski, E., Förster Schreiber, N. M., Fossati, M., et al. 2019, ApJ, 886, 124, doi: [10.3847/1538-4357/ab4db8](https://doi.org/10.3847/1538-4357/ab4db8)
- Xu, X., Heckman, T., Henry, A., et al. 2022, ApJ, 933, 222, doi: [10.3847/1538-4357/ac6d56](https://doi.org/10.3847/1538-4357/ac6d56)
- Xu, X., Henry, A., Heckman, T., et al. 2022, The Astrophysical Journal, 933, 202, doi: [10.3847/1538-4357/ac7225](https://doi.org/10.3847/1538-4357/ac7225)
- . 2023, The Astrophysical Journal, 943, 94, doi: [10.3847/1538-4357/aca89a](https://doi.org/10.3847/1538-4357/aca89a)
- Zhu, G. B., Comparat, J., Kneib, J.-P., et al. 2015, The Astrophysical Journal, 815, 48, doi: [10.1088/0004-637X/815/1/48](https://doi.org/10.1088/0004-637X/815/1/48)